



Fluid-Structure Interaction Simulations of a Tension-Cone Inflatable Aerodynamic Decelerator for Atmospheric Entry

R.M.J. Kramer¹

University of Illinois at Urbana-Champaign, Urbana, IL 61801.

F. Cirak²

University of Cambridge, Cambridge, CB2 1PZ, UK

C. Pantano³

University of Illinois at Urbana-Champaign,

1206 W. Green St., Urbana, IL 61801.

We discuss a series of fluid-structure interaction simulations of an aerodynamic tension-cone supersonic decelerator prototype intended for large mass payload deployment in planetary explorations. The fluid-structure interaction computations combine large deformation analysis of thin-shells with large-eddy simulation of compressible turbulent flows using a loosely-coupled approach to enable quantification of the dynamics of the vehicle. The simulation results are compared with experiments carried out at NASA Glenn Research Center. Reasonably good agreement between the simulations and the experiment is observed throughout a deflation cycle. The simulations help to illuminate the details of the dynamic progressive buckling of the tension-cone decelerator that ultimately results in the collapse of the structure as the inflation pressure is decreased. Furthermore, the tension-cone decelerator exhibits a transient oscillatory behavior under impulsive loading that ultimately dies out. The frequency of these

¹ Post-doctoral associate, Department of Mechanical Science and Engineering.

² University Lecturer, Department of Engineering.

³ Associate Professor, Department of Mechanical Science and Engineering, Associate Fellow AIAA

oscillations was determined to be related to the acoustic timescale in the compressed subsonic region between the bow shock and the structure. As shown, when the natural frequency of the structure and the frequency of the compressed subsonic region approximately match, the decelerator exhibits relatively large non-axisymmetric oscillations. The observed response appears to be a fluid-structure interaction resonance resulting from an acoustic chamber (piston like) mode exciting the structure.

I. Introduction

The concept of the inflatable aerodynamic decelerator (IAD) was first proposed in the 1960's as an alternative to conventional parachute technologies for decelerating payloads during the atmospheric entry phase of the entry-descent-landing (EDL) sequence of a planetary exploration mission (see [1] for a broader history of the IAD concept). Numerous proposals and mission profiles for use of IAD technologies have been developed for vehicle entry into the atmospheres of Earth, Mars, Titan, and the gas giants, e.g., [2-5]. In these studies, the key advantage of the IAD is its low mass to drag-producing area ratio, which reduces the ballistic coefficient of the entry vehicle and increases its deceleration rate at high planetary altitudes, where atmospheric density is low. This permits higher elevation landing sites to be considered and/or the landing of higher mass payloads. Additionally, the resulting aerodynamic heating is reduced, enabling the use of modern lightweight materials [6]. Preliminary experimental investigations also indicate that inflatable decelerators may avoid the well-known instabilities encountered by supersonic parachutes for high-mass payloads in the Mach number range of interest [7]. Together, these benefits offer a potential reduction in total mission weight and cost. But first, the complex coupled dynamics of these inflatable flexible structures in supersonic flows must be better understood to rule out potential instabilities.

To date, the development of inflatable decelerator concepts has been largely confined to conceptual studies and reduced-scale, often rigid model, wind tunnel testing to investigate the fundamental aerodynamic properties of different geometries and proposed designs. Recent Earth-atmosphere descent tests [8, 9] have made a significant contribution, and further experiments are ongoing [10, 11],

but for deployment as a mission-ready technology, a better understanding of the aerodynamics and aeroelastic behavior of these flexible structures is needed [12]. The most relevant experimental study to the present work is that of Clark et al. [13], where a flexible scale model was tested in a supersonic wind tunnel under a range of flow conditions. Static aerodynamic coefficients were collected and inflation/deflation cycles investigated. These experiments revealed drag hysteresis, where collapse of the decelerator structure was observed at a lower inflation pressure than that at which deployment occurred.

High-fidelity computational modeling of inflatable aerodynamic decelerators has been limited [14, 15], due to the challenging flow regime and the complexity of coupling fluid and structural solvers in an accurate and computationally efficient manner. Few computational results have been published for aerodynamic decelerators in the high-speed regime [16, 17], as opposed to the lower-speed regime, e.g., [18–21]. Recent developments in compressible turbulence modeling and structural thin-shell modeling have led to development of new fluid-structure interaction simulation tools, which can properly capture interactions between the flexible decelerator and its wake. Our recent work simulating supersonic parachutes [22] laid the foundation for the present work by providing a computational framework suitable for investigating dynamics of flexible membrane structures undergoing large deformations in a turbulent compressible supersonic flow. IAD concepts include a wide range of ballute geometries, but the focus of this paper will be a particular variant of the tension-cone geometry similar to that studied in [3] and [13]. In this vehicle, a tension-cone membrane is attached to the shoulder of the payload vehicle and supported on its outer edge by a flexible pressurized toroid that acts as a compression ring. The shape of the tension-cone is chosen such that the circumferential stresses are relatively small in comparison to the meridional stresses (at zero angle of attack). Inflation of the torus initiates the deployment of the decelerator structure.

A detailed parametric study of the dynamics of a tension-cone inflatable decelerator model is conducted in this paper using state-of-the-art fluid-structure interaction simulation. A structured grid adaptive mesh refinement (AMR) approach is employed by the fluid dynamics solver along with a compressible large-eddy turbulence model to accurately model the turbulent flow around the vehicle [23]. This is coupled using a loosely-coupled staggered approach with a large-deformation

thin-shell finite-element solver that incorporates an elastic conservative self-contact model [24–26]. The resulting fluid-structure interaction analysis tool is used to investigate the stability and aerodynamic behavior of the tension-cone decelerator at varying torus inflation pressures and under different flow conditions, with particular attention given to the transient dynamics of buckling and collapse of the decelerator and interactions with its wake. Comparison will also be made with the experimental wind tunnel test results of [13]. Finally, we extended the simulation parameters beyond those used in the experiment to drive the IAD into a resonant state and investigate a unique nonlinear fluid-structure interaction mode discovered in this device.

II. Inflatable Aerodynamic Decelerator

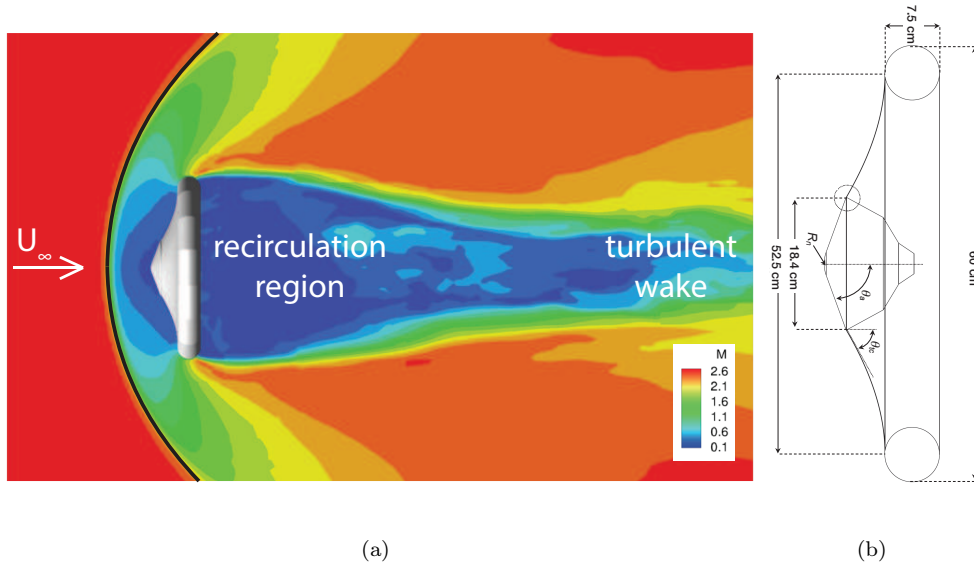


Fig. 1 Closeup of the flow (a) and cross-section of tension-cone geometry (b) indicating major dimensions of the 60 cm scale model used in [13] and the present computational study. The capsule is a scaled-down Viking-type model, with $R_n = 4.74$ cm and $\theta_a = 70^\circ$. The tension-cone meets the capsule at an angle $\theta_{tc} = 60^\circ$ (in its stress-free state).

Figure 1 shows Mach number isocontours of a domain cross-section at one set of flow conditions (a) and details of the inflatable experimental model investigated in [13], the cross-section of which is shown in (b). The tension-cone decelerator is characterized by an outer toroid, inflated to a pressure p_T that is controlled by an independent pneumatic circuit, which supports an approximately conical membrane attached to the shoulder of a capsule-type vehicle [13]. The supersonic flow, with

freestream velocity U_∞ and Mach number M_∞ , is characterized by a bow shock upstream of the vehicle and a turbulent wake behind. The large recirculation region immediately behind the tension-cone decelerator is defined by flow separation that occurs approximately at the location of maximum diameter of the vehicle. Because this is a blunt object, flow separation is abrupt and it is not very sensitive to the geometrical details of the structure. In the present study, the vehicle model is a scaled-down version of the Viking-type design. The capsule has a diameter of 18.4 cm at the shoulder where the cone is attached, an aeroshell angle of 70° , and a nose radius of 4.74 cm; see Fig. 1(b). The capsule surface is approximated by a triangular mesh that is then used to construct a level set on the fluid grid that defines the region occupied by the interior of the capsule. This is considered as a rigid body and is fixed in space. Our model lacks the support structure (balance) used to hold the device in place in the wind tunnel experiments, against which the simulation results will be compared, and it represents more accurately a free-flight configuration. Nevertheless, the support structure is installed behind the capsule in the wake of the IAD where its contribution to drag and flow behavior is known to be small for supersonic and hypersonic flight. More importantly, the experimental test article contains inflation tubes that are used to control the pressure in the torus. These were not modeled presently since sufficient geometrical details were not provided in [13] and their contribution to drag and inflation pressure deployment uncertainty was not completely documented. The outer diameter of the tension-cone model is 60 cm and the torus has a diameter of 7.5 cm. The tension-cone and torus are modeled as thin shells. The connection between the cone and torus is assumed to be fixed, such that the common edges of the finite-element triangles that discretize both surfaces remain connected as the structure deforms while they are free to rotate relative to each other. On its opposite end, the cone is fixed to the rim of the rigid and stationary capsule. The thin shell has a thickness of 0.254 mm and a linear elastic isotropic material model is assumed with a Young's modulus of 13.5 GPa and a density of 1440 kg/m³ [27].

Figures 2(a) and (b) show the model that closely approximates the geometry of the inflatable experimental model shown in Fig. 1(b). The tension-cone is a 16-sided polygon with an outer diameter of 60 cm across the flat sides of the polygon. Its meridional profile matches the nominal design of the experimental model, which was determined using linear membrane theory and CFD

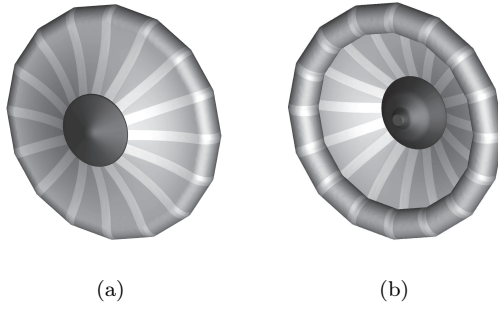


Fig. 2 Front and back views of the IAD structural model of the experimental geometry (16-sided polygon) (a,b). Light regions highlight the seams between segments of the polygon, which are modeled with twice the thickness of the interior regions.

results under the constraint of zero circumferential stress in the tension-cone [13]. At the capsule attachment point, the half cone angle is 60° . An additional detail included in this model is the presence of seams at the intersections of the segments forming the polygonal cone. These have a width of 2.54 cm, extend through the cone and torus, and are prescribed to have twice the thickness of the interior material. The seams are highlighted in Fig. 2 (a) and (b) with lighter shading. The two inflation tubes used in the experimental test article to control the torus pressure are not included in the computational models. As observed in the experiments of [13], the attachment points of the tubes present weak points in the torus and the folds may preferentially initiate from these points, an effect that will not be captured in this study. The tension-cone and torus are modeled as thin shells and discretized with a triangular unstructured mesh of 84,560 elements. The material model for this geometry has zero Poisson's ratio. The choice of zero Poisson's ratio is a compromise to better approximate the anisotropic behavior of the urethane-coated Kevlar[®] fabric material used in the experimental model.

III. Computational Models and Approach

A. Fluid Modeling

The tension-cone decelerator is a blunt body in a supersonic (compressible) flow, which is characterized by the presence of a large turbulent wake. At the Reynolds numbers of interest, on the order of 10^6 , resolution of all length scales in the flow is computationally infeasible. To accurately represent the turbulent flow and the influence of unresolved length scales, a large-eddy simulation (LES) model is employed.

The Favre filtered Navier-Stokes equations provide separation between the large scales of the simulated flow and the small scales modeled. The Favre or density-weighted filtering operator is defined by

$$\tilde{f} = \frac{\overline{\rho f}}{\bar{\rho}}, \quad (1)$$

where f is an arbitrary field, ρ is the density and the overbar indicates the conceptual filtering operation implied in LES. The modeling assumptions of negligible subgrid viscous work and triple correlations leads to the LES governing equations for the density $\bar{\rho}$, momentum $\bar{\rho}\tilde{\mathbf{u}}$, and total energy \bar{E} . The subgrid contributions are modeled by the stretched vortex model [28, 29]. This model provides expressions for the subgrid-scale stress tensor,

$$\tau_{ij} = \bar{\rho}(\widetilde{u_i u_j} - \tilde{u}_i \tilde{u}_j) \approx \bar{\rho} \tilde{k} (\delta_{ij} - e_i^v e_j^v), \quad (2)$$

and the subgrid-scale heat transport flux,

$$q_j = \bar{\rho}(\widetilde{c_p T u_j} - \tilde{c}_p \tilde{T} \tilde{u}_j) \approx -\bar{\rho} \frac{\Delta_c}{2} \tilde{k}^{1/2} (\delta_{ij} - e_i^v e_j^v) \frac{\partial(\tilde{c}_p \tilde{T})}{\partial x_j}, \quad (3)$$

where δ_{ij} denotes the Kronecker delta, Δ_c the cutoff scale of the LES, \tilde{c}_p the resolved specific heat at constant pressure, and \tilde{T} denotes the temperature. The ideal gas equation of state for air is used. The subgrid-scale kinetic energy, \tilde{k} , is estimated by assuming a spiral vortex form [30], according to

$$\tilde{k} = \int_{k_c}^{\infty} E(k) dk, \quad (4)$$

where $k_c = \pi/\Delta_c$ represents cutoff wavenumber of the LES (to be discussed shortly), and \mathbf{e}^v is the unit vector aligned with the subgrid vortex axis, here taken as the direction of the eigenvector associated with the largest eigenvalue of the resolved rate-of-strain tensor \tilde{S} , and $\nu = \bar{\mu}/\bar{\rho}$ is the kinematic viscosity. The subgrid-scale vortex represents the ensemble of vortical filaments contributing to the subgrid stresses [31]. The energy spectrum for the subgrid motion has the form

$$E(k) = K_o \epsilon^{2/3} k^{-5/3} \exp[-2k^2 \nu / (3|\tilde{a}|)], \quad (5)$$

where k is the wavenumber, K_o is the Kolmogorov prefactor, ϵ is the local cell-averaged turbulence dissipation (resolved and subgrid scale) and $\tilde{a} = \tilde{S}_{ij} e_i^v e_j^v$ is the axial strain along the subgrid vortex.

The model is completed by estimating $K_o \epsilon^{2/3}$ which equal $\overline{\mathcal{F}_2}(\Delta)/(\Delta^{2/3}A)$ [28, 32], where $A = 4 \int_0^\pi s^{-5/3}(1 - \sin s/s)ds \approx 1.90695$, Δ denotes the grid spacing, and

$$\overline{\mathcal{F}_2} = \frac{1}{6} \sum_{j=1}^3 \sum_{i=1}^3 [\delta_j(\tilde{u}_i^+)^2 + \delta_j(\tilde{u}_i^-)^2], \quad (6)$$

denotes the resolved second-order structure function for velocity. In (6), $\delta_j(\tilde{u}_i^\pm)^2 = \tilde{u}'_i(\mathbf{x} \pm \mathbf{e}_j \Delta) - \tilde{u}'_i(\mathbf{x})$ denotes the velocity increment along the corresponding coordinate direction (with unit vectors \mathbf{e}_j). Further details of this model can be found elsewhere [33]. The main enhancement with respect to the previously published stretched-vortex model is the development of the corrected velocity \tilde{u}'_i , which is introduced to minimize the incorrect activation of the subgrid-scale model at shock locations. Evaluating (6) with the fully resolved velocity $\tilde{\mathbf{u}}$ at or near a shock will result in abnormally large values of ϵ , due to the large gradient in the velocity around a shock. Therefore, any mean coherent wave component (such as a shock) is removed from the velocity field by a least-square fitting procedure before calculating $\overline{\mathcal{F}_2}$ in (6). The strategy is to decompose the velocity field according to

$$\tilde{\mathbf{u}} = \tilde{\mathbf{u}}' + \mathbf{b} \cdot \mathbf{x}', \quad (7)$$

where \mathbf{b} denotes a vector (with three components) that is determined by a least-squares fit over the 26 grid cells surrounding the cell for which the subgrid-scales stresses is being calculated, and \mathbf{x}' denotes the spatial coordinates with respect to the center of the cell in question. This strategy exploits the fact that a numerically captured shock will appear in the simulation as an approximately-uniform sharp-gradient zone that may be inclined at an arbitrary angle with respect to the frame of reference. This non-turbulent flow feature can be removed with modest computational cost. The fluctuations over the uniform gradient zone are more representative of turbulence activity and they are therefore used in (6). Consequently, the shocks appear smooth to the subgrid-scale model and the LES is not strongly activated there. The strategy to adapt the LES model and make it aware of the presence of shocks is a compromise that produced good results in our simulations; with minimal subgrid-scale model activation around the bow shock ahead of the IAD (note that there are no complex shock-shock interactions in the flows simulated here).

To optimize computational efficiency, a structured-grid dynamic AMR discretization of the flow

domain is utilized [34], which offers a reduced computational cost compared to a unigrid finite-volume technique [23]. The cutoff scale Δ_c was selected to be the local grid spacing Δ of the finest mesh at each location with a smooth transition at the locations where a fine mesh resides next to a coarse mesh. The level of mesh refinement was controlled by refinement criteria described in § IV.

The governing equations are discretized in space using a second-order accurate conservative finite-difference method with low numerical dissipation and time advancement uses a third-order Runge-Kutta method [23]. A hybrid discretization approach is used to simulate turbulence using LES and shock capturing. In turbulent and smooth flow regions, e.g., irrotational regions, a non-dissipative central-difference scheme (in stable skew-symmetric form) is used, while in regions where shocks are present, a finite-difference weighted-essentially non-oscillatory (WENO) scheme is used to accommodate flow discontinuities. These finite-difference stencils are tuned to minimize dispersive errors at the interfaces between the different schemes. The selection between centered or WENO scheme is accomplished by a nonlinear detection algorithm [35]. The algorithm analyzes the flow and determines the locations where the nonlinear Rankine-Hugoniot jump conditions are satisfied. These regions are then marked for discretization with the WENO scheme and the remainder of the flow is left for the centered method. The PhD. thesis of Lombardini provides full details on the implementation [35].

B. Structural Modeling

The tension-cone and the torus of the inflatable decelerator are modeled as thin-shells using Kirchhoff-Love theory. Due to the extreme thinness of the considered membrane materials, the bending stiffness of an inflatable decelerator is significantly smaller than its membrane stiffness. However, the bending stiffness plays a crucial role in the determination of the arrangement and amplitude of the wrinkles and folds on the shell. As is well known, simply neglecting the bending stiffness leads to the formation of an infinite number of wrinkles of vanishing amplitude [36]. To circumvent this problem, membrane models based on the tension-field theory have been proposed [36, 37]. Tension-field theory, however, can only predict the stress state in the membrane and not the detailed deformation state. The out-of-plane deformations of the membrane, which can only be

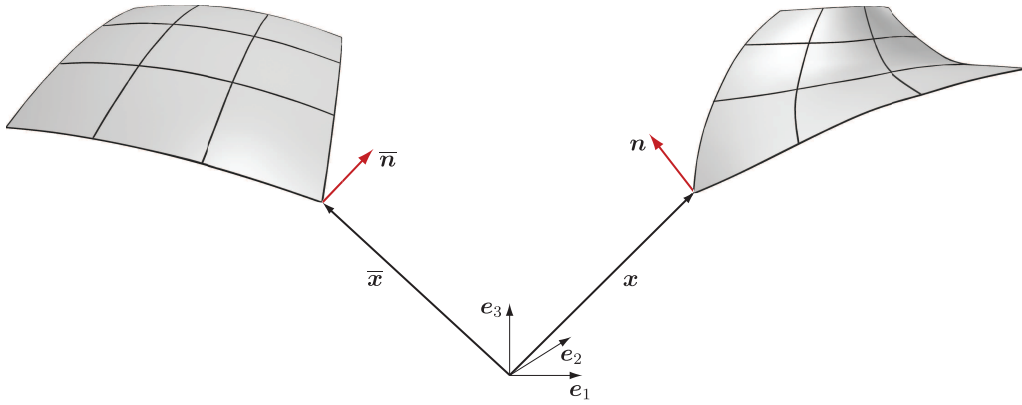


Fig. 3 Shell mid-surface in the reference and the deformed configurations (left and right, respectively).

predicted with a shell theory, are crucial for the fluid-dynamics at the fluid-structure interface. From a computational viewpoint, for the considered large-scale structures, the mesh resolution required to resolve all wrinkling is computationally prohibitive [38, 39]. Therefore, the element sizes used in the present computations are larger than the smallest possible wrinkling wave length. Nevertheless, the present approximations are adequate to capture the essential dynamics of the structure.

The Kirchhoff-Love theory does not consider the out-of-plane shear deformations of the shell and is particularly well suited for modeling thin shell structures. Details of the specific shell theory used are described in [24, 25, 40], which are briefly summarized here. Any configuration of the shell is assumed to be defined as

$$\boldsymbol{\varphi} = \mathbf{x} + \xi \mathbf{n}, \quad \text{with } -\frac{\ell}{2} \leq \xi \leq \frac{\ell}{2}, \quad (8)$$

where $\boldsymbol{\varphi}$ is the position vector of a material point within the shell volume, \mathbf{x} is the position vector of a material point on the mid-surface Ω , \mathbf{n} is the unit normal to the mid-surface, ξ is the thickness coordinate and ℓ is the shell thickness. A Lagrangian description is used, where quantities with a bar denote reference configuration variables and quantities without a bar denote current (or deformed) configuration variables, see Figure 3.

The equilibrium equation of the shell in its weak form can be written as

$$G_{\text{dyn}}(\ddot{\mathbf{x}}, \delta \mathbf{x}) + G_{\text{int}}(\mathbf{x}, \delta \mathbf{x}) - G_{\text{ext}}(\mathbf{x}, \delta \mathbf{x}) = 0, \quad (9)$$

where the first term is the contribution of the inertial forces

$$G_{\text{dyn}}(\ddot{\mathbf{x}}, \delta \mathbf{x}) = \int_{\bar{\Omega}} \rho_s \ddot{\mathbf{x}} \cdot \delta \mathbf{x} d\bar{\Omega}, \quad (10)$$

and ρ_s denotes the mass density of the surface, $\ddot{\mathbf{x}}$ the acceleration of the material points on the mid-surface, and $\delta \mathbf{x}$ the virtual deformations (i.e., test functions). The integration domain $\bar{\Omega}$ is the shell mid-surface in the reference configuration. The inertia terms associated with the rotation of the shell normal have been neglected as they are very small for thin shells. Further, the virtual work of the internal forces can be written as consisting of a membrane and a bending part

$$G_{\text{int}}(\mathbf{x}, \delta \mathbf{x}) = \int_{\bar{\Omega}} \left(\mathbf{N} : \frac{\partial \boldsymbol{\alpha}}{\partial \mathbf{x}} + \mathbf{M} : \frac{\partial \boldsymbol{\beta}}{\partial \mathbf{x}} \right) \cdot \delta \mathbf{x} d\bar{\Omega}, \quad (11)$$

where \mathbf{N} is the stress resultant tensor, $\boldsymbol{\alpha}$ is the conjugate membrane strain tensor and the operator $:$ denotes the trace operation. Similarly, \mathbf{M} is the moment resultant tensor and $\boldsymbol{\beta}$ is the respective conjugate bending strain tensor. The strain tensor $\boldsymbol{\alpha}$ depends on the first-order derivatives and the strain tensor $\boldsymbol{\beta}$ on the second-order derivatives of the reference and deformed shell mid-surface $\bar{\mathbf{x}}$ and \mathbf{x} , respectively. In computing the stress and moment resultant tensors from the corresponding membrane and bending strain tensors we assume a linear elastic isotropic material model. For the exact definition of stress and strain resultant tensors and the constitutive equations we refer to [24, 25].

In the present computations, the external virtual work is due to instationary fluid pressure loading

$$G_{\text{ext}}(\mathbf{x}, \delta \mathbf{x}) = \int_{\bar{\Omega}} p \mathbf{n} \cdot \delta \mathbf{x} d\bar{\Omega}, \quad (12)$$

where p is the scalar fluid pressure, which may vary in space and time. The pressure loading is always in the direction of the shell normal and hence orthogonal to the mid-surface.

The conforming finite element discretization of the internal virtual work (11) requires shape functions with square integrable second-order derivatives (because of the second-order derivatives present in $\boldsymbol{\beta}$). In the present work, smooth subdivision surfaces, as introduced in [24], have been used as finite element shape functions. Subdivision surfaces can be understood as the generalization of splines to unstructured meshes and are identical to splines on structured meshes, see [40] for

details. The particular subdivision scheme employed is the Loop subdivision scheme which operates on triangle meshes. As in standard finite elements, integrals (10), (11) and (12) are expressed as the sum of element integrals and the reference and deformed mid-surface position vectors, $\bar{\mathbf{x}}$ and \mathbf{x} , and the test function $\delta\mathbf{x}$ are discretized with subdivision shape functions. Subsequent numerical integration of the element integrals with one integration point per triangle and the assembly of the element contributions into global matrices and vectors yield the semi-discrete equations of motion of the shell

$$\mathbf{M}_{\text{dyn}}\ddot{\mathbf{x}}_h + \mathbf{f}_{\text{int}}(\mathbf{x}_h) - \mathbf{f}_{\text{ext}}(\mathbf{x}_h, t) = 0. \quad (13)$$

Here, $\ddot{\mathbf{x}}_h$ and \mathbf{x}_h are the acceleration and position vectors, respectively, and \mathbf{M}_{dyn} is the mass matrix, \mathbf{f}_{int} is the internal force vector and \mathbf{f}_{ext} is the external force vector. The dimension of the vectors and matrices in (13) is such that it includes all the nodes in the entire finite element mesh. Moreover, notice that in (13) the nodal positions \mathbf{x}_h of the deformed mid-surface mesh are the only degrees of freedom. Different from traditional shell elements no rotational degrees of freedom are present. Such so-called rotation-free shell elements are very appealing for problems with large deformations and have also been developed using alternative approaches, see e.g., [41–43].

The semi-discrete equations of motion (13) are integrated in time with the explicit Newmark scheme in a predictor-corrector form. Assuming that at time t^n the coordinates \mathbf{x}_h^n , the velocities $\dot{\mathbf{x}}_h^n$ and the accelerations $\ddot{\mathbf{x}}_h^n$ of the finite element nodes are known, the corresponding vectors at time $t^{n+1} = t^n + \Delta t$ are predicted with

$$\mathbf{x}_h^{n+1} = \mathbf{x}_h^n + \Delta t \dot{\mathbf{x}}_h^n + \frac{1}{2} \Delta t^2 \ddot{\mathbf{x}}_h^n, \quad (14a)$$

$$\dot{\mathbf{x}}_{h,\text{pre}} = (1 - \gamma_{\text{Newmark}}) \Delta t \ddot{\mathbf{x}}_h^n + \dot{\mathbf{x}}_h^n, \quad (14b)$$

where γ_{Newmark} is the Newmark damping parameter (with $0.5 \leq \gamma_{\text{Newmark}} \leq 1$) and $\dot{\mathbf{x}}_{h,\text{pre}}$ is the predictor velocity. Subsequently, the final velocities follow from

$$\ddot{\mathbf{x}}_h^{n+1} = \mathbf{M}_{\text{dyn}}^{-1} (\mathbf{f}_{\text{ext}}(\mathbf{x}_h^{n+1}) - \mathbf{f}_{\text{int}}(\mathbf{x}_h^{n+1})), \quad (15a)$$

$$\dot{\mathbf{x}}_h^{n+1} = \dot{\mathbf{x}}_{h,\text{pre}} + \gamma_{\text{Newmark}} \Delta t \ddot{\mathbf{x}}_h^{n+1}. \quad (15b)$$

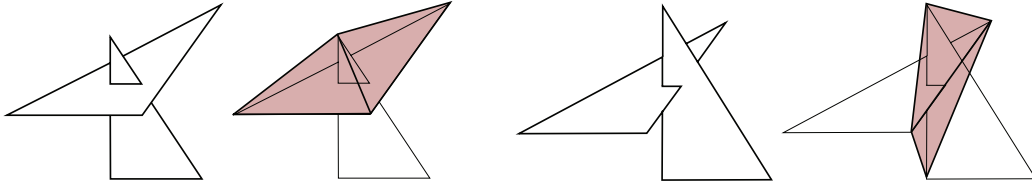


Fig. 4 Possible triangle-triangle penetrations and the definition of the constraint function $g(\mathbf{x}_h)$. The left two figures illustrate vertex-triangle penetration and the right two figures illustrate edge-edge penetration. The volume of the coloured tetrahedrons represents $g(\mathbf{x}_h)$.

In computations, the mass matrix \mathbf{M}_{dyn} is diagonalized with the row-sum technique, i.e. the elements of each row are summed together and assigned to the diagonal. The resulting diagonal mass matrix can be trivially inverted.

For the tightly folded tension-cone configurations, the motion of the surface mesh resulting from the time integration may lead to collisions between the surface elements. To remedy this, penetrations that occur after the predictor update (14) are identified and subsequently resolved by considering collision equations. To this end, a geometric indicator function $g(\mathbf{x}_h)$, which depends only on the nodal positions in the deformed configuration, is introduced. The indicator function is $g(\mathbf{x}_h) \leq 0$ for admissible configurations and $g(\mathbf{x}_h) > 0$ for inadmissible configurations with penetration. For deformations where contact has just occurred, it is $g(\mathbf{x}_h) = 0$. Although it is possible to define the indicator function $g(\mathbf{x}_h)$ in terms of global geometric quantities, such as intersection volumes, it is advantageous to define it using local quantities only. In the present application, essentially two different type penetrations are possible: either a node penetrates a finite element, or the edge of a finite element penetrates the edge of another element; see Figure 4. In both cases the indicator function is defined as the signed volume of the tetrahedron formed by one triangle and a vertex, or by two edges, respectively.

If, after the predictor update (14), an inadmissible configuration with penetration is detected, it is resolved in two steps. First, the penetrations are removed by modifying the predictor positions \mathbf{x}_h^{n+1} using closest point projections. In our implementation, in the node-triangle penetration case the penetrating vertex is simply projected back to the closest point on the triangle surface. Similarly, in the edge-edge impact case the penetrating edge is projected to the closest point on the triangle

edge. Subsequently, the predictor velocities (14b) of the finite element nodes participating in the collision are modified so that the kinetic energy and momentum during the collision is conserved.

As derived in [26] this can be accomplished with the following update formula

$$\dot{\mathbf{x}}_{h,\text{pre}}^+ = \dot{\mathbf{x}}_{h,\text{pre}} - 2 \left(\frac{\nabla \mathbf{g} \cdot \dot{\mathbf{x}}_{h,\text{pre}}}{\nabla \mathbf{g}^T \mathbf{M}_{\text{dyn}}^{-1} \nabla \mathbf{g}} \right) \mathbf{M}_{\text{dyn}}^{-1} \nabla \mathbf{g}, \quad \text{with } \nabla \mathbf{g} = \frac{\partial \mathbf{g}}{\partial \mathbf{x}_h}. \quad (16)$$

Here, $\dot{\mathbf{x}}_{h,\text{pre}}^+$ is the post collision predictor velocity, which inserted into the Newmark corrector (15b) yields the velocity for the new time step. In our implementation, the collision removal and update (16) are performed by removing one-by-one all node-triangle and edge-edge penetrations until a geometrically admissible mesh configuration is obtained.

C. Fluid-Structure Coupling

The fluid-structure interaction is modeled using a loosely-coupled staggered approach [44, 45]. The fluid and structural models interact in computational terms only in a thin region around the interface boundary using a temporal splitting method. This interaction is modeled using a variant of the Ghost-Fluid Method (GFM) [46] introduced in [47–49]. In this technique, the fluid state in the cells covered (overlapped) by the solid are reconstructed with values that satisfy the velocity slip boundary conditions at the location of the interface between solid and fluid. These reconstructed cells are referred to as ghost cells and a level set technique is used to represent the solid boundary in the Cartesian fluid solver.

The GFM concept is sketched in Fig. 5(a). First, the solid geometry is converted into a level set (a signed distance function). Second, the computational cells are divided into two groups: those with positive distance function are labeled fluid cells (lower left-hand side in Fig. 5(a)) and those with negative distance function are labeled ghost cells (upper right-hand side). The flow vector of state at the ghost cells, the red point in Fig. 5(a), is obtained from the state in the mirrored fluid side, the closest specular location to the ghost cell with respect to the boundary (blue point). Interpolation is used to reconstruct the state at the mirrored points inside the fluid domain since they do not coincide, in general, with the coordinates of the center of the fluid cells. Recall that, as introduced in Section III A the flow vector of state has five components $(\bar{\rho}, \bar{\rho} \tilde{\mathbf{u}}, \bar{E})$. In a third and final step, the normal velocities in the ghost cells is set to $-(\tilde{u}_i n_i) n_j$, while the tangential velocity

remains unmodified. Here, normal and tangential components are defined with respect to the normal of the solid boundary n_i computed as the gradient of the level set function. The modified normal velocities in the ghost cells approximatively enforce a reflective type boundary condition at the solid boundary. After the ghost region is suitably populated, the fluid solver introduced in Section III A is applied without modification of the numerical stencils. See [47–49] for further details.

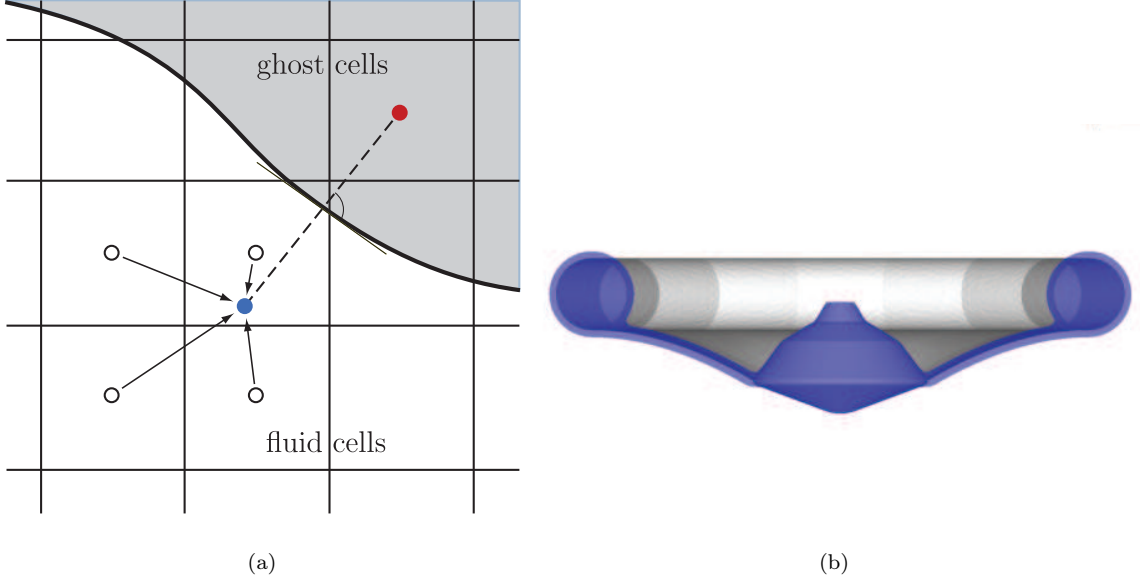


Fig. 5 Conceptual sketch of the Ghost Fluid Method (a) and cross-section of the tension-cone model with the ghost fluid region highlighted. Note the thickening of the thin tension cone, but not of the torus and solid rigid capsule (b).

In the present IAD application, the fluid interacts with a thin-shell mid-surface thickened by $\tau\Delta$, where $\Delta = (\Delta x\Delta y\Delta z)^{1/3}$ is the characteristic cell size and $\tau \approx 1.75$. This regularizes the thin shell to a thickness that can be resolved by the Cartesian discretization of the flow equations. Figure 5(b) shows a cross section through the tension-cone model with the ghost region highlighted on the slice that indicates thickening of the thin tension-cone shell and the torus. The interior of the torus is identified as a special ghost region, where the desired inflation pressure is specified independently of the exterior fluid flow. No attempt is made to resolve the flow inside the torus region and it is modeled as a homogeneous ideal gas.

The fluid pressure on each shell finite element node is evaluated as the difference between the fluid pressure on shells top surface and the fluid pressure on its bottom surfaces, p^+ and p^-

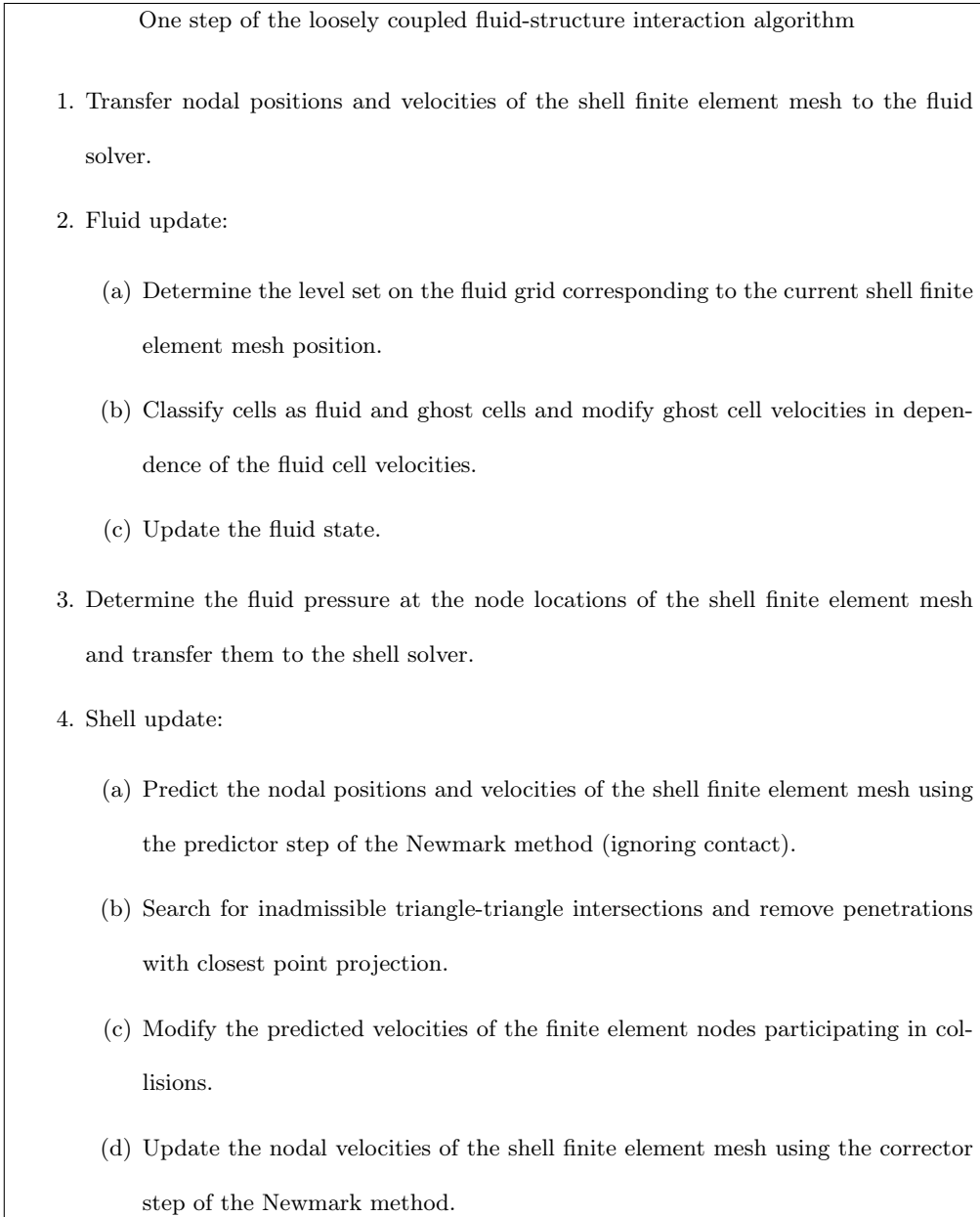


Fig. 6 Algorithm for coupling the shell solver with the fluid solver using the ghost-fluid method.

respectively. It is assumed that the shell mesh is oriented so that a unique definition of a top and bottom surface is possible. The solid boundaries satisfy the slip boundary condition, essentially an inviscid approximation, while the pressure and density satisfy the zero normal gradient condition. We neglect the small subgrid pressure forces that are not resolved by the subgrid closure used in the present LES. This boundary condition is applicable in the present flow because the forces induced by high-speed flows over blunt objects are mostly due to pressure; shear stresses are relatively

small. This is verified in comparison with the experiments below. In our case, the separation of the boundary layers, formation of the recirculation region and wake behind the capsule and tension cone, are rather well defined due to the blunt geometry of the structure. There is still structural coupling with the flow because the pressure fluctuations generated in the turbulent wake are radiated everywhere, and in particular towards the structure, where they couple with its dynamics. Therefore, both mean pressure behavior and pressure fluctuations from the strong turbulent wake are felt by the structure. Further discussion of the applicability of this boundary condition for highly-compressible separated flows can be found in [22].

IV. Simulation Results

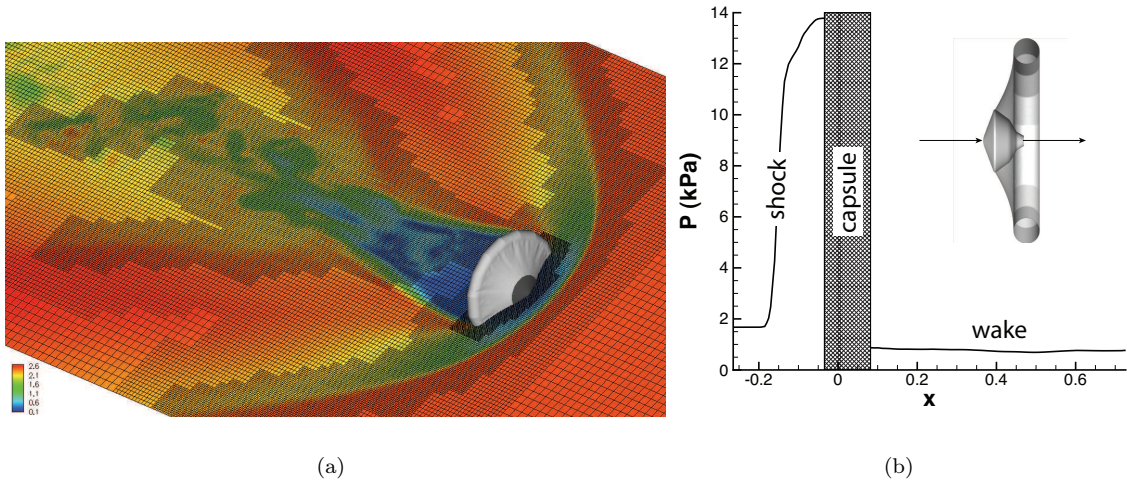


Fig. 7 Slice through the center of the computational fluid domain showing regions of mesh refinement, superimposed on contours of Mach number (a); the torus is inflated to a pressure of 300 kPa. Variation of pressure along the axis of symmetry of the tension-cone decelerator (b); inset indicates the line from where the pressure was measured and the shaded region in the figure indicates the solid portion of the capsule.

The flow conditions described in the experimental campaign correspond to a stagnation pressure of 28.63 kPa with a free stream Mach number of 2.5 and velocity of $U_\infty = 311.4$ m/s, for a Reynolds number of 1.6×10^6 [13]. The dynamic pressure $q = 1/2 \rho U_\infty^2$ was 153 psf. All torus inflation pressures quoted in the following are absolute in kPa. To aid in the discussion of the multiple simulations we keep the units of kPa for inflation pressures and psf for dynamic pressures. The computational

flow domain is a box of dimensions $12 \times 3 \times 3$ meters and is discretized dynamically using AMR with three additional levels of refinement at a refinement factor of 2 between levels. The cells at the fluid-structure interface are always refined to the maximum level. The finest cell size is 5.8 mm and the total fluid mesh size is approximately 40 million cells, varying slightly with time as refinement evolves to accommodate flow features and the deformation of the structure. Refinement is primarily localized near the body and the bow shock; an instant of a slice through the center of the domain superimposed onto contours of Mach number and mesh density is shown in Fig. 7(a). Resolution needs at these conditions was established in previous FSI simulations [22]. The flow direction is aligned with the x coordinate direction and the face of the tension-cone decelerator lies nominally in the y - z plane. Figure 7(b) shows the variation of the pressure along the line that coincides with the axis of symmetry of the tension-cone decelerator. Note that the shaded area indicates the solid body of the capsule. One can observe in this figure the presence of the bow shock, the compressed region between the shock and the nose of the capsule, where the pressure increases by more than eight times the free-stream value, and the wake behind the vehicle. The large pressure difference between the nose and back of the capsule, on the order of 13 kPa, is the main contributor to the drag of the IAD; variations in the radial direction are also present (not shown in the this one-dimensional view).

The structural model is initialized in the simulation without accounting for any (locked-in) pre-stress due to fabrication of the experimental test vehicle. The flow is initialized by a shock wave upstream of the structure. The thermodynamic and flow conditions are determined by solving the corresponding one-dimensional Riemann problem. A clean shock wave (without rarefactions) travels towards the tension-cone decelerator and sets the upstream flow at its desired conditions. The initial condition completely washes out of the computational domain within 40 ms of physical time. The parametric investigation of the response of the structure to varying inflation pressure followed the following quasi-static protocol. First, a simulation was initialized at high p_T and the flow was allowed to develop to a fully turbulent state over 100 ms. All initial conditions were washed out and the flow became statistically stationary. The inflation pressure was then lowered in small steps of 25 kPa and the flow was again allowed to reach statistically steady conditions.

A. Startup transient and steady fully inflated results

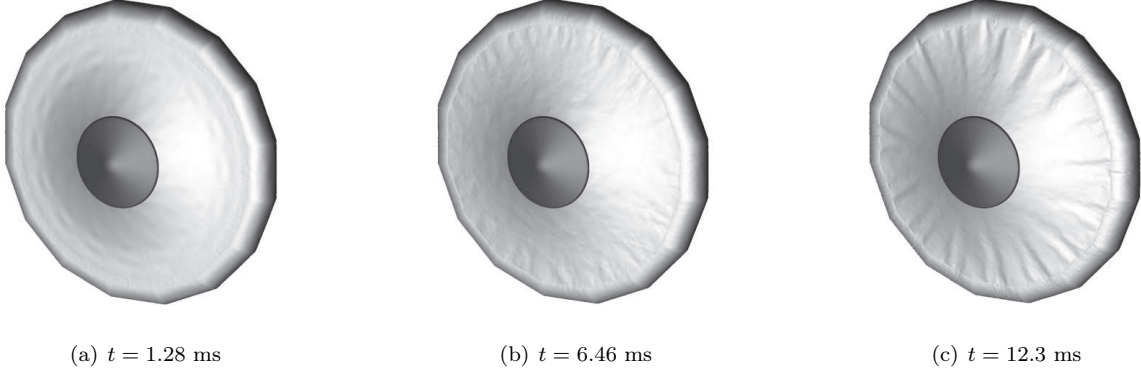


Fig. 8 Structure at three different instants during the initial transient of the simulation, at a torus inflation pressure of 350 kPa.

Figure 8 depicts the polygonal tension shell, with the torus inflated to 350 kPa (a high pressure), at three instants during the initial transient of the simulation. As indicated earlier, the simulation is started with the structure in the deployed position but without any pre-stress due to fabrication. As the initial flow-starting shock travels over the tension-cone it transfers an impulse to the structure, Fig. 8(a), that leads to the formation of a small-amplitude circumferential out-of-plane wave that travels across the tension-cone. This ripple quickly decays and is replaced by the appearance of stationary radially aligned wrinkles of the cone surface. As can be seen in Fig. 8(c), the comparatively less stiff mid-span of each polygonal torus segment deflects further than its adjacent stiffer corners. This leads to the appearance of compressive strains in the cone which in turn leads to wrinkling. At this inflation pressure and early time in the simulation, the torus displays minimal deformation.

After the initial transient settles, a fully developed flows arises, shown at one instant as Mach number contours on the x - y plane for a torus inflation pressure of 350 kPa in Fig. 9. Principal features of this turbulent supersonic flow include the curved bow shock, the turbulent wake and low-speed region directly behind the tension-cone decelerator, and recompression shocks downstream of the wake. The minimal distance between the bow shock and the nose of the capsule is approximately 13.2 cm, the wake is turbulent and a low-pressure recirculation zone exists directly behind the capsule. The cyclic symmetry of the structure combined with the thicker seam regions also prevents, to a significant extent, the development and propagation of small-amplitude high-frequency out-of-plane

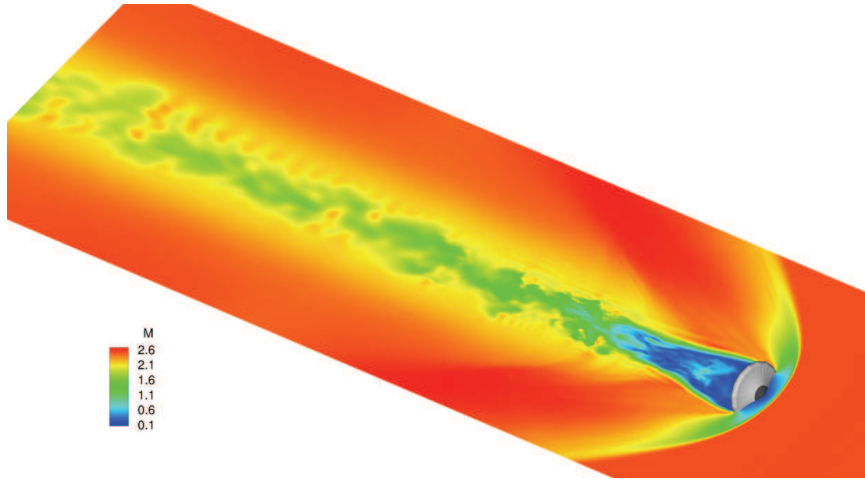
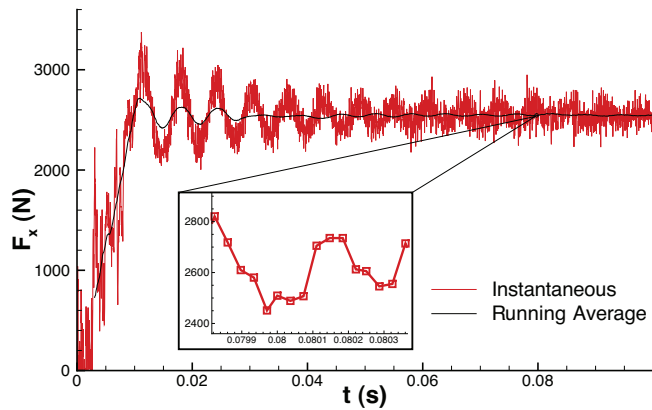
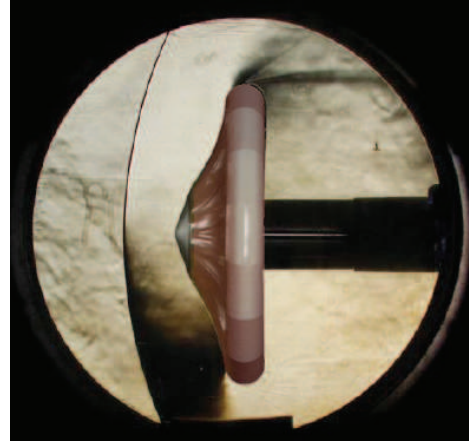


Fig. 9 Slice through the center of the computational fluid domain showing contours of Mach number for fully developed flow over the polygonal tension-cone geometry. The torus is inflated to a pressure of 350 kPa.

waves that feed energy from the coupling with the fluid. Comparison of the structure, after the transients has died down, with Fig. 8(c) at 12.3 ms shows that there is little change over time when the torus is fully inflated. At the later time in particular, deformation of the tension-cone is limited to very small amplitude wrinkling of the surface.



(a)



(b)

Fig. 10 Axial force with the torus fully inflated to 350 kPa, from initialization of the simulation (a) and side view of an overlay of the computational and experimental structure (b).

To gain further insight into the dynamics of the fully deployed tension-cone decelerator, Fig. 10(a) shows the instantaneous axial (drag) force on the combined capsule and tension-cone

decelerator over 100 ms, from start-up of the simulation. Also shown is a running average of the force with a window of 5 ms, which eliminates the very high frequency stochastic oscillation that is a result of structural feedback with small-scale turbulence in the flow. From a negligible initial value, the force on the structure rises quickly as the dynamic pressure load on the tension-cone increases through the initial transient. A decaying oscillatory transient is observed as the flow develops, resulting in a drag force fluctuation about what later becomes its mean value. The initial impulse exerted by the shock and subsequent flow development causes the tension-cone decelerator to move back and forth in the axial direction, with the torus remaining mostly in a y - z plane. This axial oscillation is damped out by the fluid and dies out almost completely after 60–70 ms. It is notable that during deployment experiments conducted by [13], an overshoot in the axial force through the inflation transient was reported that is similar to the overshoot seen in Fig. 10(a) (which is on the order of 6–7%). The dynamics of the polygonal tension-cone decelerator are essentially those of a rigid body once the axial oscillation has decayed and the structure is settled in an equilibrium configuration. The inset in figure 10(a) shows a zoom around $t = 80$ ms, where the individual values of the drag extracted from the simulation at each time step are shown with symbols (the time step was approximately $4.6 \mu s$ and was determined by the variable time-step controller of the Runge-Kutta integrator to maintain a Courant number below 0.7). This inset highlights the time-resolved nature of the simulation and clarifies that what appear as substantial variations of the drag with time observed in the larger scale figure are a consequence of coupling with the turbulent flow, which possesses these very fine time-scale features itself. Figure 10(b) shows a side view overlay of the computational structure, after the initial transient, with a Schlieren photograph in [13]. It can be seen that the deformed structure superimposes qualitatively well over the photograph of the experiment. Note that the comparison is only approximate because there is no accurate photogrammetry measurement from where we could compare the simulation quantitatively. In addition, the shock standoff distance is measured to be approximately 12.6 cm that is within approximately 4% error of the computationally measured value of 13.2 cm. These comparisons establish within reasonable tolerances the validity of the simulation results in the steady regime.

Figure 11 shows the evolution of the axial force for three different resolutions in the nominal

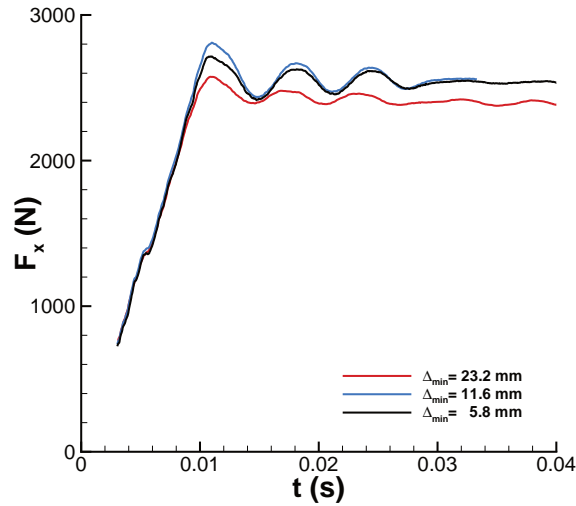
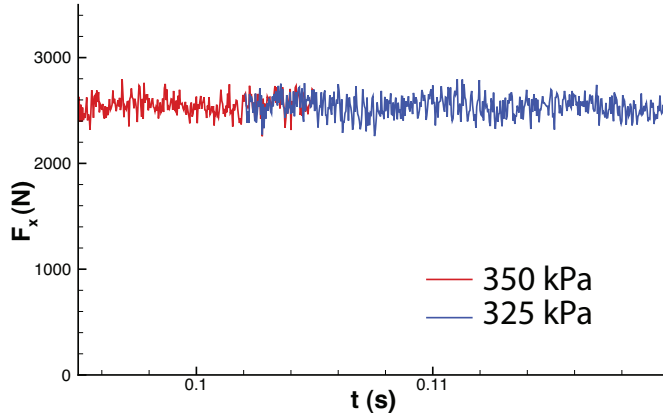


Fig. 11 Running average of the axial force with the torus fully inflated to 350 kPa for three different grids at resolutions increasing from 2 to 4 levels or AMR.

inflated torus at 350 kPa. The simulations have identical conditions but the number of levels of AMR was varied from 2 to 4 to study grid convergence of the solution. The simulations have a finest grid spacing of $\Delta = 23.2, 11.6,$ and 5.8 mm, respectively. As can be seen in the figure, the solution on the coarsest resolution mesh displays marked deviations with respect to the next finer simulations while the two finer meshes produce results that are very close. In consequence, we believe that the finest mesh resolution used in this study is very close to converged and we have used this resolution in the remainder of the analysis.

B. Deflation Simulation Sequence

After the flow and structure achieved statistically steady-state conditions, we proceeded to lower the pressure of the torus in a quasi-static manner. The dynamics of the tension-cone decelerator under decreasing torus inflation pressure were examined by performing a sequence of simulations at progressively lower pressures until the structure collapsed. The sequence began with the torus fully inflated to 350 kPa that had run for 100 ms to ensure that the flow was fully developed after the initial transient. The simulation was then continued with the inflation pressure lowered progressively in steps of 25 kPa, running at each new pressure value for 50 ms. The pressure reduction was instantaneous; *i.e.*, a step function. After each change of inflation pressure, a short



(a)

Fig. 12 Drag evolution after a step change in inflation pressure from 350 kPa to 325 kPa.

transient develops that lasts for about 10 ms before a new statistically-steady state is reached. In the results that follow, all force coefficients reported are based on data from the latter 40 ms of each run. Figure 12 shows the evolution of the drag after the step change in inflation pressure from 350 kPa to 325 kPa. As can be seen in this figure, the response of the mean drag is very smooth after the change in inflation pressure. This supports our choice for the 25 kPa step change in inflation pressure to conduct the deflation sequence. Note that, as seen in the figure, we kept running the simulation at 350 kPa for a short while to compare with the run at the lower inflation of 325 kPa. There are no appreciable differences in the drag during and after the inflation pressure change but we chose to systematically discard the first 10 ms after a pressure inflation change to ensure no spurious data (albeit small) was left over in the results.

Figure 13 shows the tension-cone structure at the end of the simulation periods for different inflation pressures through the deflation simulation sequence. Reduction of the inflation pressure by 100 kPa, from 350 kPa to 250 kPa, has relatively little effect on the stability of the structure as the torus remains nearly fully inflated. Further reduction of the pressure leads to a buckling of the torus, which settles into a post-buckled state with about eight localized folds (half the number of sides of the polygon). These folds are located near the mid-spans of segments of the polygonal structure, away from the stiffer corner regions, and increase in amplitude as the inflation pressure decreases. At 125 kPa, Fig. 13(e), the deformation starts to focus at two hinge-like folds on the torus and large-scale symmetric bending type deformation of the tension-cone and torus are apparent. The

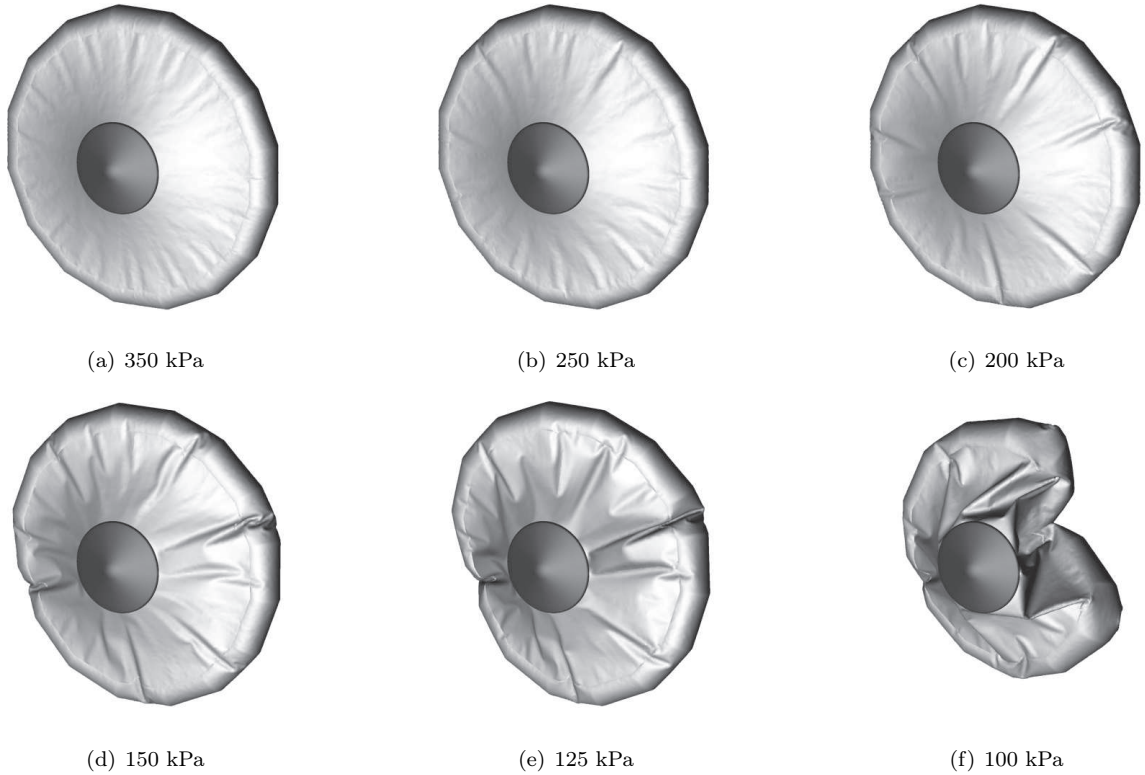


Fig. 13 Snapshots of the tension shell state at different torus inflation pressures from the simulation sequence with decreasing inflation pressure.

structure does not collapse until the pressure is reduced further, to 100 kPa. Note that the collapsed configuration shown in Fig. 13(f) is one among many possible. The particulars of the computational analysis, the deflation history and flow around and behind the tension-cone decelerator will select a particular collapsed state.

Axial (drag) force coefficients for the combined capsule and tension-cone decelerator system through the deflation sequence are plotted in Fig. 14, and the corresponding tangential (lift/yaw) force coefficients are shown in Fig. 15. These mean force coefficients are calculated from the latter 40 ms of each 50 ms simulation and the latter 50 ms for the first simulation that run for 100, and error bars show the standard deviation of each computational value. When fully inflated, the axial force coefficient of the system is $C_A = 1.21 \pm 0.05$, while the forces in directions perpendicular to the flow direction are small, $C_T = 0.005 \pm 0.076$ (as expected at the present zero angle of attack). Note that the standard deviation is an order of magnitude larger than the average force, which is very nearly zero. The collapsed system is found to have an axial force coefficient of $C_A = 0.64 \pm 0.05$,

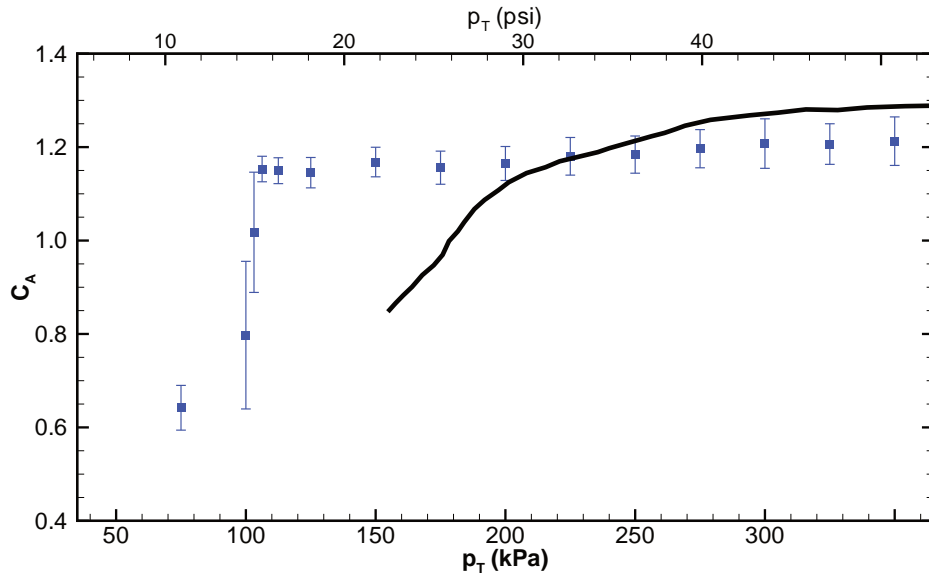


Fig. 14 Average axial force coefficients on the combined capsule and tension-cone decelerator with varying torus inflation pressure. Continuous curve denote experimental results and discrete datapoints denote simulation results with vertical bars denoting the standard deviation of the fluctuations.

and tangential force coefficient $C_T = -0.040 \pm 0.040$. The variation in the forces on the vehicle is primarily a function of the projected surface area of the tension membrane, so the coefficients reported for the collapsed structure are strongly dependent on its particular configuration. Note also that the larger tangential force is due to the asymmetry of the collapsed structure. For comparison, the experiments of [13] reported an axial force coefficient of approximately $C_A = 1.3$ for the fully inflated torus, and a minimum of $C_A = 0.84$ for the partially collapsed structure at the lowest inflation pressure tested in the wind tunnel. The actual drag plot obtained in the experiment is shown in Fig. 14 as the continuous curve. Note that the fully inflated result is close to the experimental value but there are differences in the drag near the nonlinear buckling regime, where all structural and mechanical differences between the experiment and the simulation contribute to the discrepancy (note that no error bars were documented in the experiment). It was noted that the reported forces are subject to some uncertainty owing to the unquantified effect of the inflation tubes used to control the torus pressure, which are not present in the simulations. This is a particularly important factor for the partially collapsed structure, where the presence of inflation tubes on the

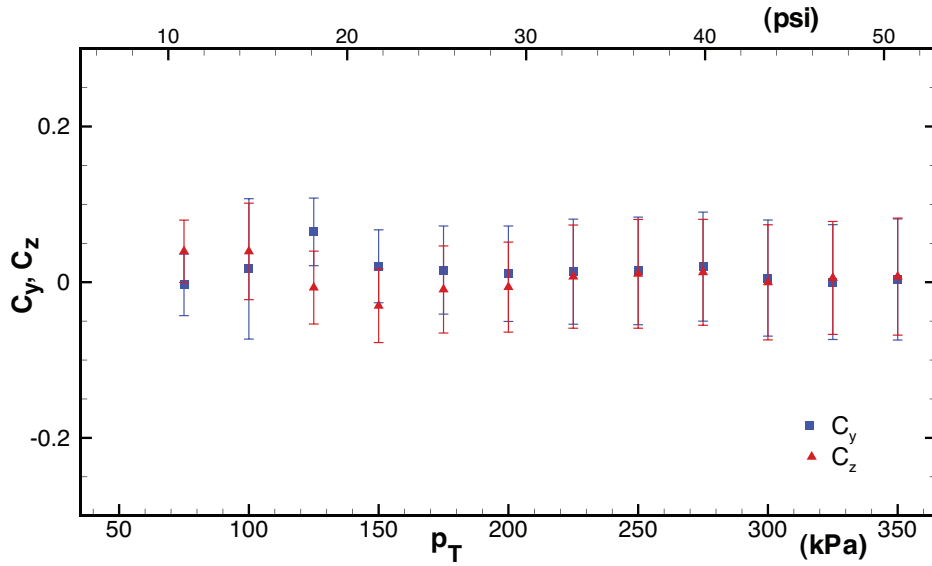
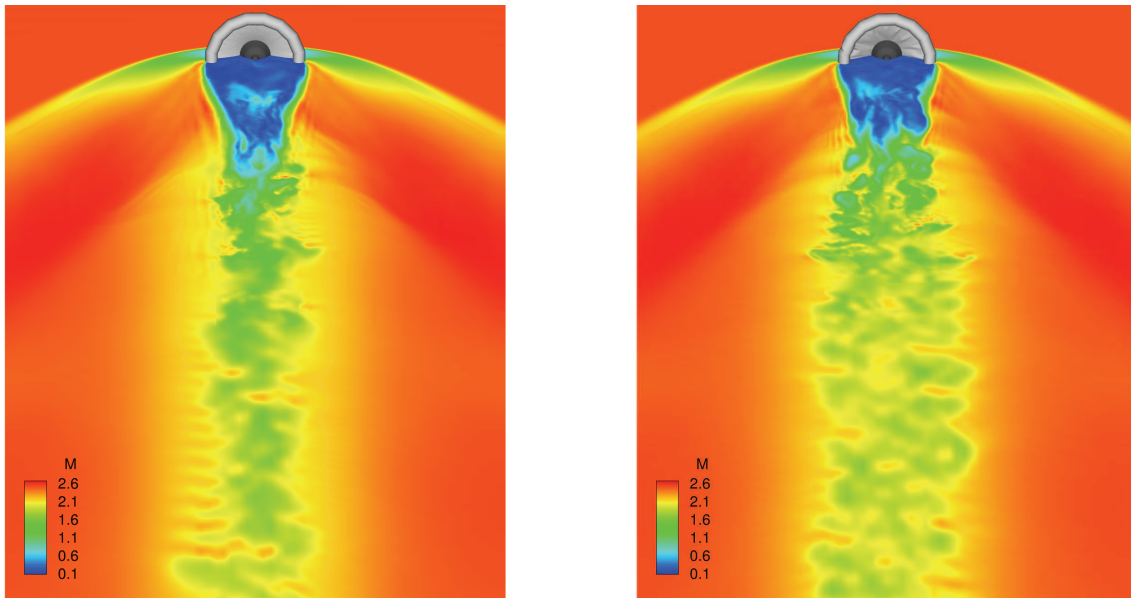


Fig. 15 Average tangential force coefficients on the combined capsule and tension-cone decelerator with varying torus inflation pressure.

experimental model resulted in a favored buckling mode where the tension-cone decelerator collapses primarily in the direction diametrically opposed to the tube axis. The experimental tension-cone decelerator is constrained by the inflation tubes and they prevent it from collapsing fully. The unconstrained structure in the present simulation collapses more extensively, and hence a lower drag coefficient (which is calculated based on the original deployed area) is to be expected.

Figures 13 and 14 show that the tension-cone structure remains stable under decreasing inflation pressure to at least 150 kPa. While the amplitude of the folds increases significantly, as seen in Fig. 13(a)–(d), the average axial force coefficient changes by little more than 5%. In terms of drag, therefore, the change in inflation pressure over this inflation pressure range has a small effect. However, a fundamental change occurs in the character of the wake, as the structure transitions from the stiff to the flexible behavior. Figure 16(b) shows that the relatively coherent wake structure observed at 350 kPa has broken up and the wake has increased significantly in width (it grows to be wider than the tension shell within about four diameters downstream).

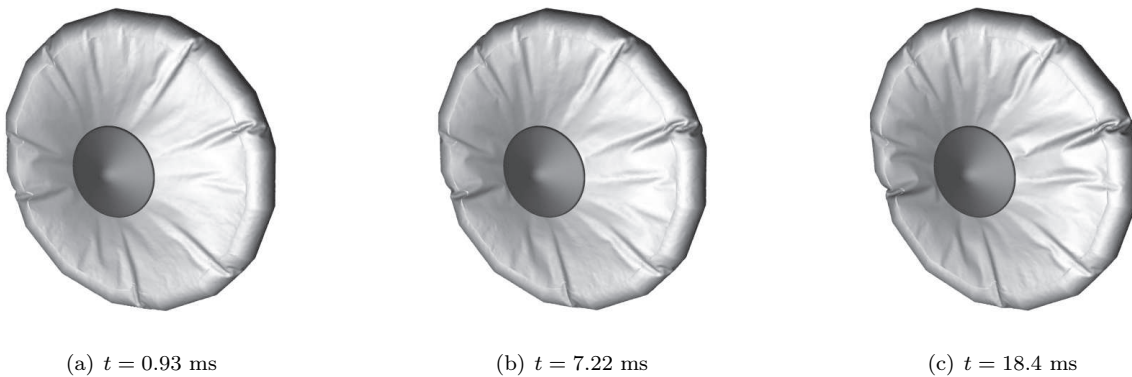
The increase in flexibility of the structure with the reduction in p_T is reflected in the increasing deformation of the tension-cone decelerator. Figure 17 shows the evolution of the surface folds over time after the torus pressure is reduced from 175 kPa to 150 kPa. The reduction in stiffness



(a) 350 kPa

(b) 150 kPa

Fig. 16 Wake comparison on a slice through the center of the domain, showing contours of Mach number, from the simulation sequence of decreasing torus inflation pressure. At the lower inflation pressure the wake has increased significantly in width.



(a) $t = 0.93$ ms

(b) $t = 7.22$ ms

(c) $t = 18.4$ ms

Fig. 17 Structure at three instants at an inflation pressure of 150 kPa. The structure stabilizes in the configuration shown in (c), undergoing only small deformations from this position after the initial transient.

of the torus leads to an increase of the compressive strains over the entire decelerator, which are accommodated by localization of the deformations in two diametrically-opposed folds. Growth of this primary buckling mode ceases as the structural forces and aerodynamic loads enter equilibrium with the tension membrane still deployed. The stability of the state shown in Fig. 17 manifests itself by the minimal further deformation over the remainder of the 50 ms simulation. The inherent

stiffness of the seam-supported polygonal shape prevents noticeable large-scale flapping or local high-frequency out-of-plane oscillations from developing, at least under the present flow conditions.

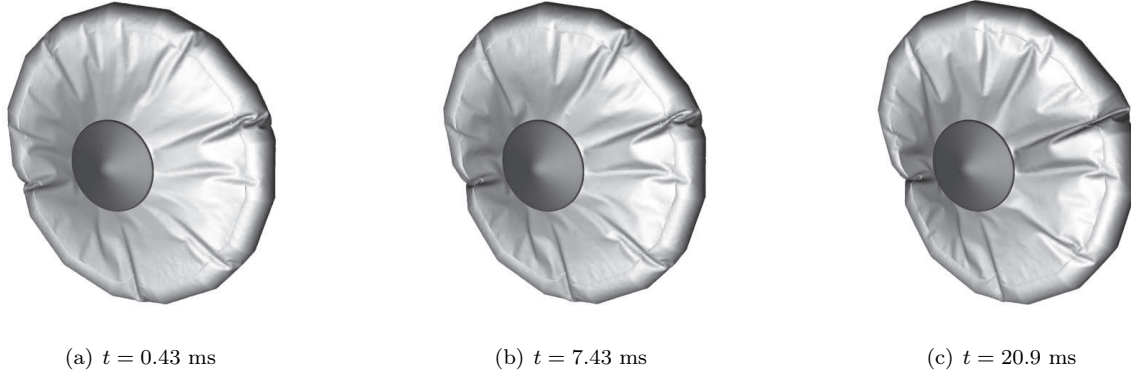


Fig. 18 Selection of structure at three instants with an inflation pressure of 125 kPa. The structure stabilizes near the configuration shown in (c), as the side with the “pinched” fold begins to flap.

As the torus inflation pressure is decreased below 150 kPa, the overall integrity of the structure starts to become compromised. Figure 18 shows the transient response of the structure to the reduction in torus pressure from 150 kPa to 125 kPa. The global buckling mode with the two hinge-like folds that started to appear at 150 kPa becomes more pronounced, but again equilibrium is reached with the structure still largely deployed. As the projected surface area of the tension-cone does not decrease significantly, the average drag coefficient drops only 2% compared to that measured at 150 kPa. The tension-cone does undergo significant deformation: one of the two large folds forming the hinge is pushed back towards the inside of the decelerator almost lying against the capsule surface, while the other fold on the opposite side becomes tighter and causes significant bending of the torus out of the y - z plane. After reaching an approximate equilibrium in the state shown in Fig. 18, the entire decelerator begins a small amplitude flapping motion, as it interacts with the wake, pivoting around the hinge formed by the two folds. The development of an asymmetry in the structure is also revealed in a significant deviation from zero in the tangential force measurement shown in Fig. 15. The flapping deformation alters the wake behind the vehicle again, as shown in Fig. 19. The low-speed region develops tails on its outer edges as slower moving vortices are shed from the flapping structure. Spreading of the wake continues as it moves downstream, and its width

increases still faster than at 150 kPa. These changes help maintain a drag coefficient within a few percent of that with the torus fully inflated, despite a reduction in frontal area of the tension-cone.

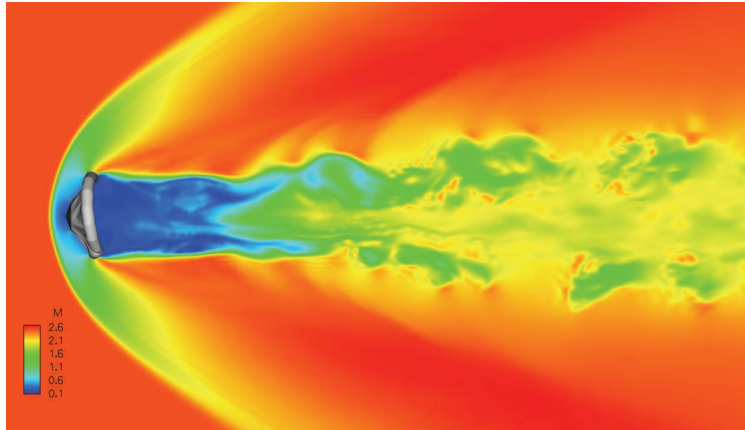


Fig. 19 Wake behind the vehicle at an inflation pressure of 125 kPa. Compared with Fig. 16, its width has increased significantly and the low-speed region has developed “tails”.

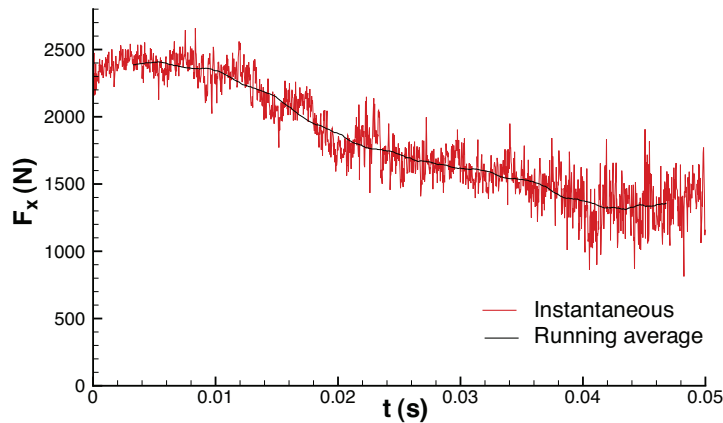


Fig. 20 Axial force acting on the vehicle after the torus inflation pressure is reduced to 100 kPa, showing the decrease in drag experienced during collapse of the tension-cone.

Further deflation of the torus to 100 kPa causes its collapse as the reduction in internal pressure is too large to withstand the compressive forces applied by the tension-cone. Figure 20 shows the development in the axial force on the vehicle, and Fig. 21 shows a sequence of the structure through collapse of the tension-cone. The initial transient response of the structure, Fig. 21(a), is a continuation of that seen at 150 and 125 kPa, as the existing folds and wrinkles grow larger in amplitude and the change in drag is minimal. The difference at 100 kPa is that an equilibrium state

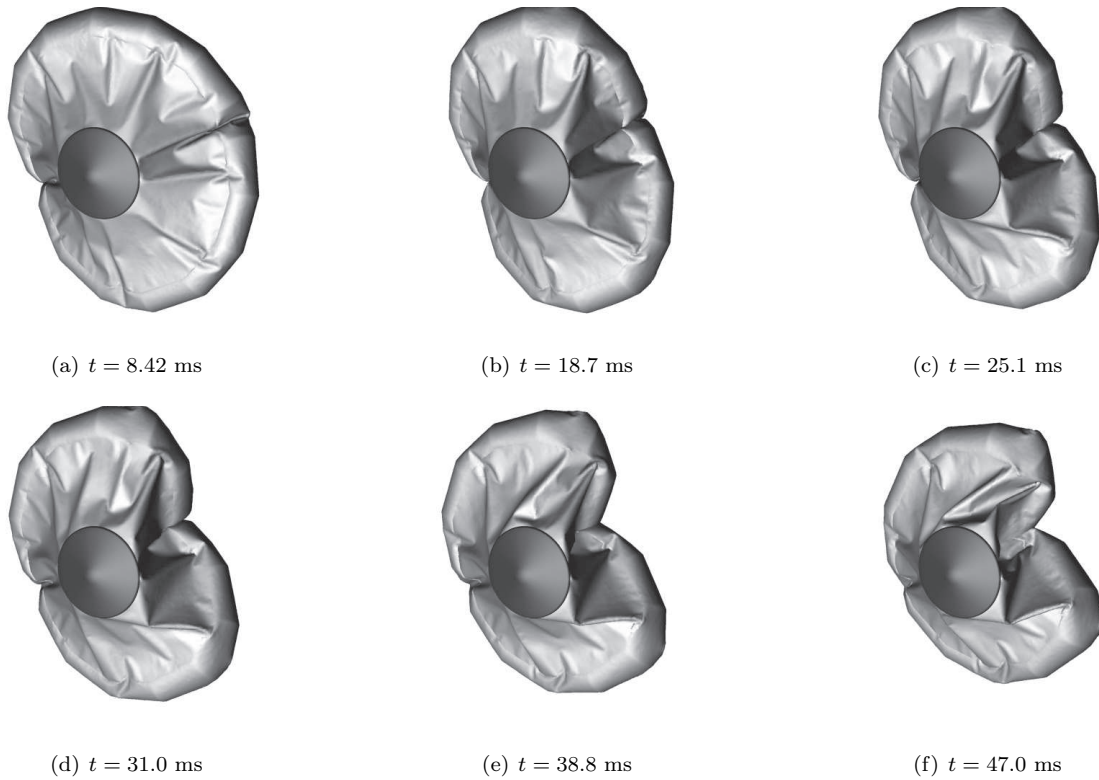


Fig. 21 Selection of structure at six instants from collapse of the tension-cone after the torus inflation pressure is reduced to 100 kPa. Note in particular the folding of the tension-cone across (a)–(c), followed by a twisting motion into the collapsed form over (d)–(f).

is not achieved; the tension-cone continues to buckle as the two hinge-like folds in the surface move rearward, (b)–(c). A large pocket forms on the right-hand side of the tension-cone (as viewed in Fig. 21) where the torus moves and becomes pinched. The next stage of collapse, (d)–(e), occurs as this side is pushed back so far towards the x-axis that it begins to pull on the opposite side in a twisting motion about the capsule and begins to form spiral folds in the tension-cone. This change to a twisting type motion enables to package the decelerator even tighter than with just radial folding possible. The resulting effect is a large reduction in the projected area of the tension-cone, which substantially reduces the drag of the vehicle over a time period of about 25 ms. The collapsed structure stabilizes into the position shown in Fig. 21(f) over the last few milliseconds of the simulation.

Further investigation of the minimal torus inflation pressure required to support the tension-cone in the deployed state was performed by running additional simulations, progressively lowering

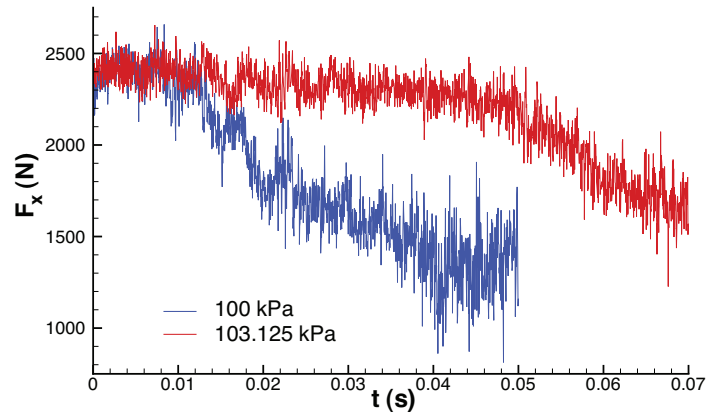


Fig. 22 Comparison of axial forces on the vehicle at low inflation pressures at which the structure collapses. Near the minimal deployment pressure, buckling occurs much more slowly.

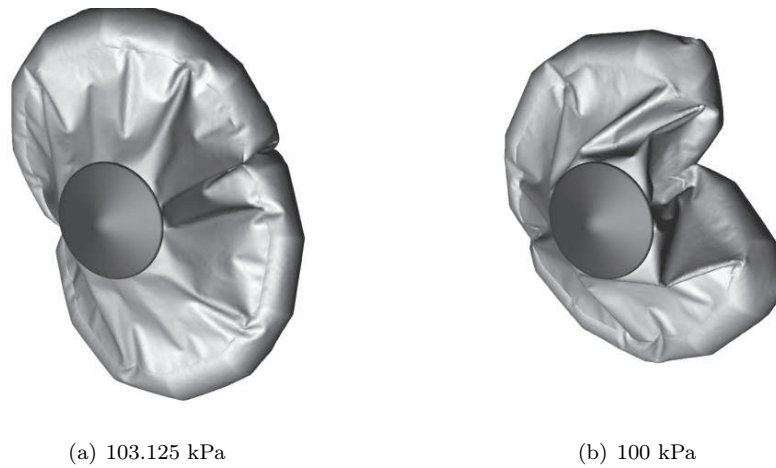


Fig. 23 Comparison of collapsed tension-cone decelerator positions, at the highest inflation pressure at which collapse was observed, and the simulation at 100 kPa, approximately 50 ms after the pressure was changed.

the inflation pressure from 125 kPa in decreasing increments until 100 kPa, where collapse was first observed. The large-scale deformation and fold growth trends observed during the simulation at 125 kPa continue when the inflation pressure is lowered to 112.5 and 106.25 kPa, but in both cases a stable deformed state is reached and the tension-cone does not collapse. Only when the pressure is further reduced to 103.125 kPa collapse is observed, with the corresponding fall in drag. The average of the pre- and post-collapse inflation pressures, 104.7 kPa, can be defined as a more accurate minimum deployment pressure. The highly nonlinear nature of the buckling process for the

tension-cone at pressures near the minimum is evident in a comparison of the collapse observed at 100 kPa with that at 103.125 kPa, shown in Fig. 22. Although differing in inflation pressure by only 3%, the speed and extent of folding of the structure after the pressure is changed is drastically different. Within 10 ms of the step change in pressure to 100 kPa, the drag on the vehicle decreases rapidly as the tension-cone begins to fold tighter undergoing an axial twisting type overall motion. A similar folding of the structure at 103.125 kPa occurs only after nearly 50 ms; before this time, deformation is limited to continued deflection of the “pinched” side of the tension-cone seen in Fig. 18(c). At 52.8 ms, the deformed structure at 103.125 kPa shown in Fig. 23(a) is in an almost identical configuration to that in Fig. 21(b). As mentioned, the geometry and location of the observed folds, the geometry of the final collapsed state and the obtained minimum deflation pressure cannot be expected to be unique. However, the present model can be used to perform parametric studies investigating the influence of different design choices, aerodynamic conditions and deflation cycles on the minimum deflation pressure.

C. Dependence of the structural collapse on the dynamic pressure

q (psf)	$p_{I,\min}$ (kPa)	$p_{I,\text{est}}$ (kPa)
153	104.7	210
100	26.6	137
50	–	68

Table 1 Minimum stable inflation pressure for the tension-cone decelerator at different dynamic pressures

To complete the examination of the tension-cone decelerator dynamics, additional simulations were performed at lower dynamic pressures. This was achieved by lowering the free-stream velocity and stagnation pressure such that the free-stream Mach number remained unchanged. Two cases were considered, relative to the baseline simulations with $q = 153$ psf: the first had a dynamic pressure of $q = 100$ psf with free-stream velocity 203.3 m/s, and the second had $q = 50$ psf and 101.7 m/s. Simulations were performed with the torus fully inflated (300 kPa) and at decreasing pressures until the structure collapsed. The minimum torus inflation pressure required to maintain

the structure in the deployed state is strongly dependent on the dynamic pressure experienced by the vehicle. The primary load on the tension-cone is the aerodynamic load across the face of the vehicle, which is proportional to the dynamic pressure in the free stream, and since that load is supported by the torus acting as a compression ring, it is directly related to the inflation pressure. To determine the torus pressure at which structural collapse occurs for the polygonal tension-cone under different dynamic pressures, the simulations at 100 and 50 psf were continued with the torus pressure progressively decreased until collapse was observed. The structure was described as collapsed if significant buckling continued after its response to the initial transient of the change in inflation pressure; this is a distinct response compared to the stably deployed tension-cone. The results of this simulation sequence are presented in Table 1. Collapse of the structure is a nonlinear process dependent on the interaction between nonlinear buckling in the torus and the aerodynamic load. Accordingly, the minimum inflation pressure varies nonlinearly with the change in dynamic pressure, increasing rapidly with increasing aerodynamic load. This pressure has been estimated by [3] by considering the minimum pressure required to reach a zero compressive stress; *i.e.*, no local wrinkling; in the walls of a circular torus. For the experimental model parameters, and assuming a drag coefficient of 1.2, the estimate, $p_{I,est}$, gives for a circular torus the values shown in the third column of Table 1. Clearly, this estimate represents only an upper bound since the nonlinearity of the structural collapse is not considered. As our simulations illustrate, the torus can undergo significant small-scale wrinkling and large-scale folding without losing its structural integrity. The minimum inflation pressure estimate is, however, in general agreement with the simulations of the polygonal tension-cone in terms of the pressure at which wrinkling of the torus begins. At 153 psf, the first small wrinkles appear in the torus at an inflation pressure of 250 kPa, but are structurally not relevant until the pressure is lowered to 225 kPa or below. The structure is not significantly compromised until 150 kPa. At 100 psf, there is no wrinkling at 150 kPa and small-amplitude folding at 100 kPa. At 50 psf, there is no folding at 50 kPa and only small-amplitude folding at 25 kPa. No collapse was observed in this simulation, even after reducing the inflation pressure to zero. It is clear from the present results that the estimate of [3] over-predicts the observed values, as the tension-cone structure remains stably deployed with significant small-scale wrinkling and even some

large-scale folding in the torus for a wide range of intermediate inflation pressures.

V. A resonant dynamical state

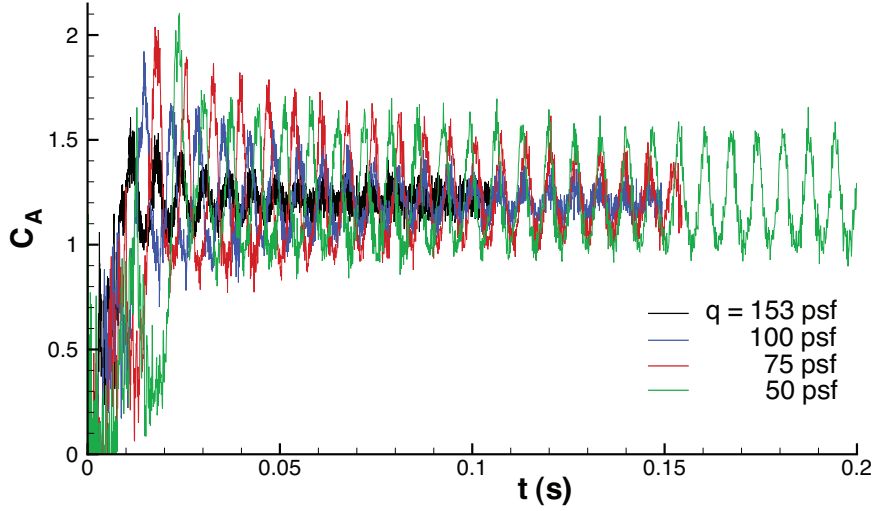


Fig. 24 Axial force coefficients acting on the vehicle at different dynamic pressures.

It was clearly observed in Fig. 10 that the passage of the initial shock over the structure, approximately a step loading, leads to sizable axial displacements of the structure (seen as oscillations in the force). At the high inflation pressure, 350 kPa, the polygonal structure experienced a transient “beating” type motion in the axial direction that decayed over 60–70 ms. Since this behavior appeared interesting, the response of the structure to the initial step loading produced by the passing shock as a function of the dynamic pressure q was explored. Several of these simulations were discussed already in Section IV C focusing on the critical inflation pressure for nonlinear buckling of the vehicle. It was observed that the amplitude of the oscillations grew as the dynamic pressure q decreased from 153 to 50 psf. To complete this data, an additional case with $q = 75$ psf and $U_\infty = 152.5$ m/s was carried out to further investigate the response of the structure. In all these cases $p_T = 300$ kPa (fully inflated). Note that the Mach number and Reynolds numbers were kept constant in these simulations but the thermodynamic conditions were adjusted as needed (excepting the case $q = 153$ psf, these new simulations are not matched to any particular experiment). Figure 24 shows the transient axial drag coefficient for all cases, $q = 50, 75, 100,$ and 153 psf. As ex-

pected, the amplitude of the oscillations in the drag increases consistently with decreasing dynamic pressure. Note that the mean steady-state value is very similar in all cases. The notable difference between each case is the amplitude of the oscillation: it increases by approximately a factor of four over the range of dynamic pressures. It appears that the cases at 75 and 50 psf have entered a near-resonant state where the interaction between the flow and the structure sustains the oscillation for a much longer period. At 100 psf, the amplitude of the oscillation in the drag is nearly a factor of two larger than that seen at 153 psf, but a self-sustaining cycle is not seen; the amplitude of the oscillation decays with time. In contrast, the case $q = 50$ psf exhibits a long sustained oscillation while the case at 75 psf shows larger initial amplitudes that decayed faster than those of the case 50 psf.

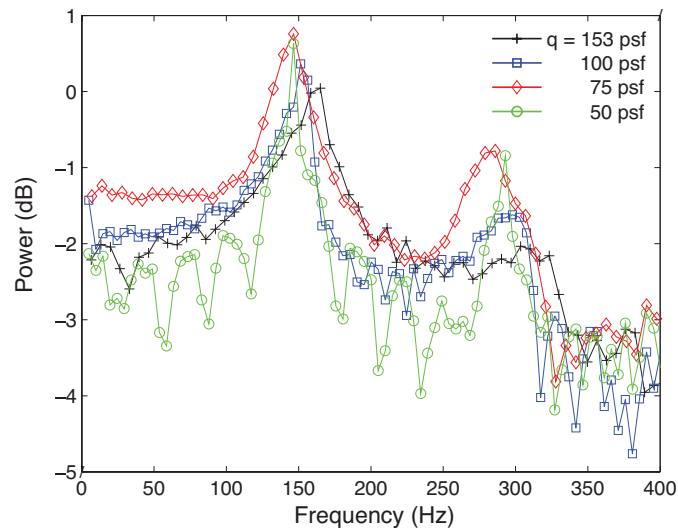


Fig. 25 Spectra of axial force after the initial transient, at various dynamic pressures for the fully inflated torus.

Fig. 25 shows the power spectra of the axial force (calculated in a window excluding the first part of the initial transient). The very clear peak occurs at the frequencies listed in Table 2 denoted by $f_{s,peak}$. In the same table, we list the mean and amplitude of the drag coefficient C_A and the acoustic frequency based on the speed of sound in the region between the bow shock and the structure, where the flow is compressed, and the distance between the nose of the vehicle and the bow shock axis of symmetry (approximately 13 cm). It is observed that the main axial mode of

q (psf)	C_A	shock distance (cm)	f_a (Hz)	$f_{s,\text{peak}}$ (Hz)
153	1.213 ± 0.052	12.70	1476	165.0
100	1.206 ± 0.092	12.79	960	151.4
75	1.221 ± 0.187	12.85	717	146.5
50	1.222 ± 0.206	13.16	465	146.5

Table 2 Acoustic frequencies in the flow and the observed structural vibrational frequencies for the axial beating mode.

vibration of the structure is approximately 150 Hz. For a given decelerator geometry, this frequency primarily depends on the material and the thickness of the structure and the inflation pressure of the torus. Minimal variation between the simulations is due to the added mass effect, which is very small in this particular case because the density of the gas is much smaller than that of the structure. As well as the fact that the inflation pressure for the case with dynamic pressure 153 psf was 350 kPa while that for the cases at 50, 75, and 100 psf simulations was 300 kPa. Examination of the spectrum for the 300 kPa inflation pressure case at the dynamic pressure of 153 psf shows a virtually indistinguishable oscillation frequency peak at 154 Hz. At 50 psf, the structure oscillation continues with a frequency of 146.5 Hz even after reduction of the inflation pressure to 150 kPa. Harmonic modes are also present, with reduced amplitude, and the first harmonic at 293 Hz is visible for both 50 and 75 psf cases in Fig. 25. The high-frequency noise evident in all the force plots presented here is incoherent but appears to lie in the frequency range 2.5–3 kHz (which was resolved with approximately 10 time steps in the simulations at 153 psf) and it is consistent with the turbulent motions in the wake behind the structure.

Figure 26 shows the structure for the $q = 50$ psf case at 157 (left half) and 160 ms (right half). These times correspond approximately to the peak and valley of an axial oscillation cycle in the fully developed flow. It can be seen that the deformation is almost entirely in the axial (x) direction and wrinkling is minimal. The maximum deflection position is approximately 4.5 mm downwind with respect to the unloaded geometry. Extrapolating from Table 2, a stronger interaction might be expected if the natural frequency of the structure were somehow increased to match the acoustic frequency of the fluid cavity enclosed by the bow shock and the front of the

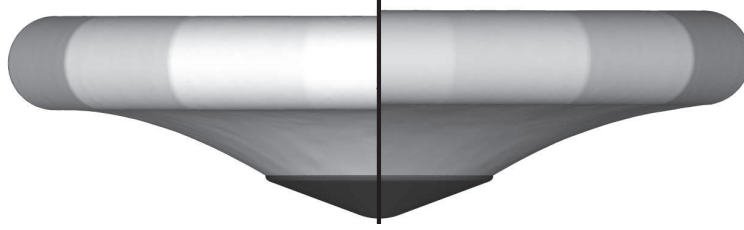


Fig. 26 Side view of the tension-cone comparing the structure at minimum (left) and maximum (right) axial deflection, showing the range of motion ($q = 50$ psf, $p_T = 300$ kPa). Artificial illumination was used in the rendering of the image to aid in the visualization of the geometry and give a natural perception of depth.

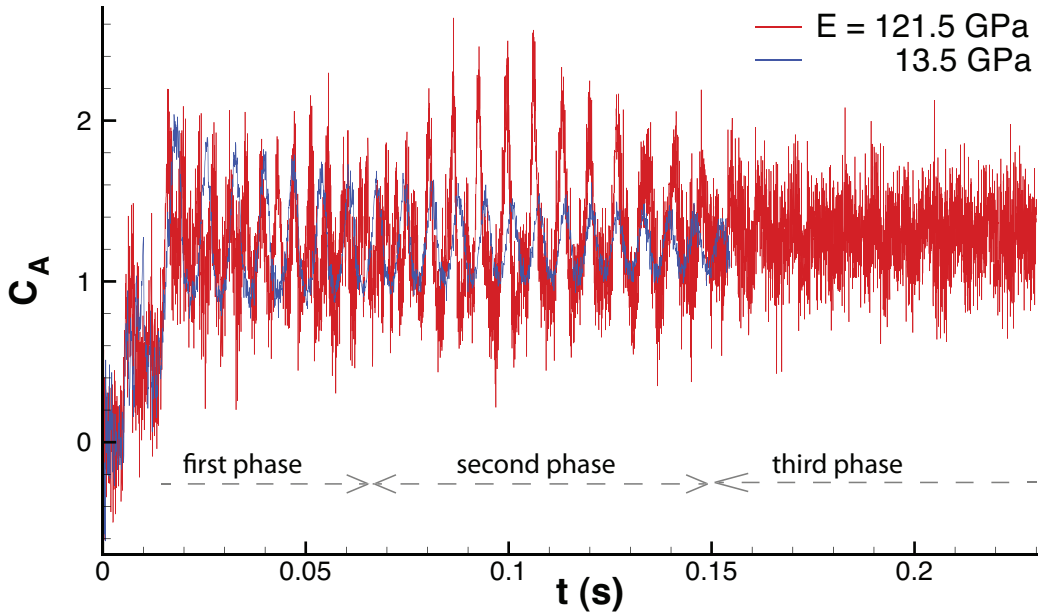


Fig. 27 Axial force coefficient comparison of simulations at $q = 75$ psf with different material Young's moduli for the tension-cone decelerator. At 121.5 GPa, the frequency of the oscillation increases and a secondary vibration develops.

vehicle. Taking as a reference case $q = 75$ psf, a natural frequency increase of the structure by a factor of four, $f_a \approx f_{s,peak}$, should match the acoustic frequency of the flow. To further investigate if a limit-cycle or resonance phenomenon is possible, an additional simulation was performed with $q = 75$ psf, but with the Young's modulus of the fabric artificially increased by a factor of nine to a value of $E = 121.5$ GPa. No claim is made that this corresponds to any particular material or condition experienced in the experiment. The rationale for increasing the Young's modulus by

this large factor was based on the observation that the longitudinal and transversal fundamental frequencies of the elastic membrane scale with \sqrt{E} , all other parameters being constant [50]. With this simple scaling, increasing the elastic modulus by a factor of nine should lead to an increase in fundamental frequencies by a factor of three, to approximately 438 Hz. As shown in Fig. 27, the increase of stiffness has a dramatic effect on the transient behavior of the structure and on the drag. In the first phase, first 60 ms of the simulation, the familiar purely axial beating is observed, though at a higher frequency. In the second phase, after the first 60 ms and before 150 ms, a new dramatic, larger amplitude, oscillation was triggered. This was sustained but appeared to be modulated and damped. In the final third phase, after 150 ms, the drag became erratic for the rest of the simulation with a very high frequency content. After some inspection of the structure and the flow, it was observed that the beginning of the second phase matches closely with the development of the turbulent flow in the wake. Before this instant, the flow is developing from its initial non-turbulent condition, but by 60 ms, small scale turbulence and coherent structures in the wake have emerged. The structural behavior after 150 ms is easily understood with the aid of the Fig. 28. As can be seen in the figure, the large axial motion in the second phase evolved under the influence of turbulent flow coupling into a growing pitching type of oscillation of the whole structure. Now, and despite the high inflation pressure, the entire torus rotates substantially along an axis that is orthogonal to the main flow direction; the maximum rotation angle of the torus reached values as large as $\pm 2^\circ$. More importantly, the side forces shown in Fig. 29 indicate that if the vehicle were to fly in these conditions it would exhibit a quite erratic trajectory.

A sketch of the fluid-structure interaction that is thought to be observed is shown in Fig. 30. The region between the bow shock and the capsule and tension-cone acts as an acoustic chamber. Here, perturbations in the displacement of the tension-cone produce acoustic waves that can propagate upstream to the bow shock wave. Part of the energy of these perturbations is reflected back to the structure, therefore closing the loop, and part is used to move the shock. There is no transmission of acoustic energy upstream of the bow shock because the flow is supersonic there. This feedback coupling results in further deformation of the structure through local displacement of the membrane but it also produces an acoustic pressure wave that becomes sufficiently strong to displace the

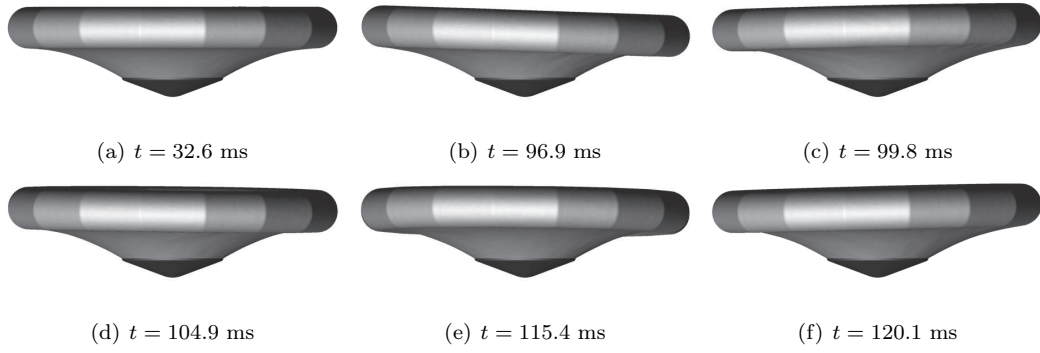


Fig. 28 Selection of structure at several instants from the simulation with the tension-cone decelerator Young's modulus increased by a factor of nine. The pairs (b)–(c), and (e)–(f), represent adjacent local axial force minima and maxima respectively, while (d) shows an intermediate state.

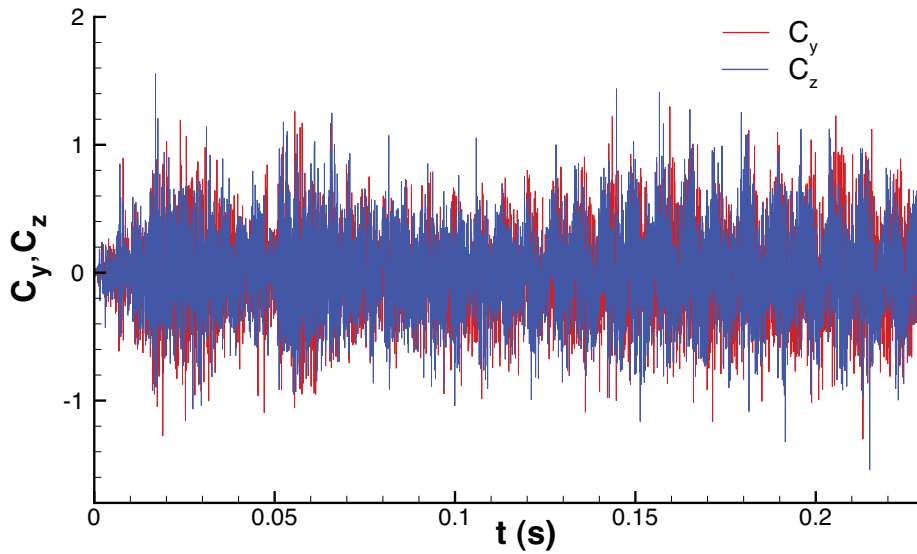


Fig. 29 Side forces of simulation at $q = 75$ psf with $E = 121.5$ GPa.

tension-cone axially. When the deformation becomes sufficiently large, the non-axisymmetric forces of the turbulent wake transfer some of the energy to excite the rotational modes of the structure (shown as spins in the figure). Note that the acoustic chamber analogy is only a partially accurate description because the bow shock, unlike a wall, is capable of displacement to satisfy the nonlinear Rankine-Hugoniot jump conditions. In our simulations, the movement of the bow shock is not appreciable until the displacements of the structure becomes large. Furthermore, some acoustic energy is radiated laterally and does not contribute to the coupling. The initial high-frequency vibration of the tension-cone membrane induces acoustic waves that travel to the bow shock and

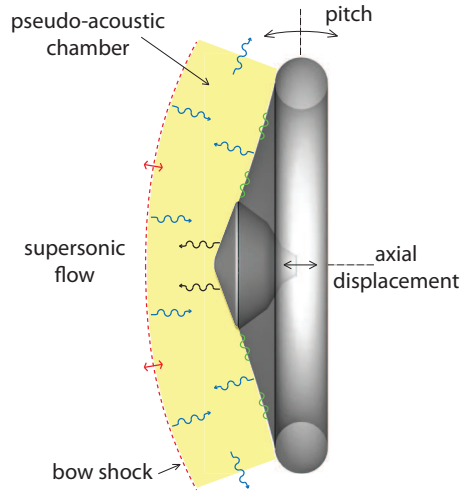


Fig. 30 Sketch of the fluid-structure coupling.

are partially reflected back towards the structure. These waves excite the structure further and lead to more transmitted energy upstream. There does not seem to be enough natural damping by viscous or turbulence diffusion to damp these acoustic waves sufficiently. As the kinetic energy of the waves and the structure keeps accumulating, with increasing structural displacements, small asymmetries originating in the turbulent wake are able to tilt (rotate) slightly the structure and induce the excitation of the relatively softer non-axisymmetric modes of deformation of the entire vehicle. Once this happens in our simulations, we presume that a strongly nonlinear coupling between the bow shock, structural dynamics, and turbulent wake maintains the cycle (third phase in Fig. 27).

VI. Conclusions

We present and discuss a number of fluid-structure interaction simulations of an inflatable aerodynamic decelerator concept for planetary exploration missions. A complete cycle of inflation pressures was performed to match experimental results available in the literature. We observe good agreement in terms of drag and deformation of the structure when the supporting toroidal structure that ensures deployment is fully inflated. As the pressure decreases, the structure collapses, in agreement with the experiment. The collapse pressure is only qualitatively matched since the computational and experimental structures are not exactly the same. An analysis of the deformed

vehicle and the dynamic phenomena that leads to the onset of buckling and the eventual collapse of the structure at low inflation pressures is discussed. It is observed that as the pressure decreases, transient localized buckling of the torus appears and disappears in a repetitive manner. As the inflation pressure decreases further, these incipient buckling regions become localized and permanent and ultimately, when the inflation pressure is sufficiently low, lead to the large-scale buckling of the structure. Changes in the turbulent wake were also observed. At high inflation pressures, the turbulent wake exhibits its well known structure with a conical (convergent) recirculation region that is straightened by a recompression shock that leads to the turbulent wake. At low inflation pressure, the wake becomes cylindrical and appears to shed coherent flow structures uniformly. No turbulent Kármán street is apparent.

Exploring the dynamic response of the structure to the initial impulsive load produced by the shock that establishes the flow, it was shown that it is possible to make the flow and structure resonate according to a new type of fluid-structure interaction resonance phenomenon. It is reasoned that the source of the resonance is a matching of the acoustic time scale, in the compressed flow region between the bow shock and the front of the vehicle, and the fundamental frequency of the structure corresponding to its axial mode of deformation. A simulation was carried out to demonstrate that such a fluid-structure coupling was indeed possible. The simulation showed that the acoustic coupling resulted in increasing displacement of the structure with time. Eventually, the deformation was so large that non-axisymmetric disturbances from the turbulent wake result in a tilt of the torus and lead to a sustained rotation oscillation that remain undamped.

Acknowledgements

This work was supported by NASA grant NNX08AL31A (technical monitor Dr. Scott Murman). The views and conclusions contained herein are those of the authors and should not be interpreted as necessarily representing the official policies or endorsements, either expressed or implied, of NASA or the US Government.

- [1] B. Smith, C. Tanner, M. Mahzari, I. Clark, R. Braun, F. Cheatwood, A historical review of inflatable aerodynamic decelerator technology development, in: 2010 IEEE Aerospace Conference, no. IEEEAC 1276, 2010.
- [2] J. P. Masciarelli, J. K. H. Lin, J. S. Ware, R. R. Rohrschneider, R. D. Braun, R. E. Bartels, R. W. Moses, J. L. Hall, Ultra lightweight ballutes for return to earth from the moon, in: 47th AIAA/ASME/ASCE/AHS/ASC Structures, Structural Dynamics and Materials Conference, no. AIAA 2006-1698, Newport, RI, USA, 2006.
- [3] I. G. Clark, A. L. Hutchings, C. L. Tanner, R. D. Braun, Supersonic inflatable aerodynamic decelerators for use on future robotic missions to Mars, *Journal of Spacecraft and Rockets* 46 (2) (2009) 340–352.
- [4] R. R. Rohrschneider, R. D. Braun, Static aeroelastic analysis of thin-film clamped ballute for titan aerocapture, *Journal of Spacecraft and Rockets* 45 (4) (2008) 785–801.
- [5] D. T. Lyons, W. R. Johnson, Ballute aerocapture trajectories at Neptune, in: AIAA Atmospheric Flight Mechanics Conference and Exhibit, no. AIAA 2004-5181, Providence, RI, USA, 2004.
- [6] F. M. Kustas, S. P. Rawal, W. H. Wilcockson, C. T. Edquist, J. M. Thornton, C. Sandy, Evaluation of high-temperature multilayer insulation for inflatable ballute, *Journal of Spacecraft and Rockets* 38 (4) (2001) 630–631.
- [7] R. R. Rohrschneider, R. D. Braun, Survey of ballute technology for aerocapture, *Journal of Spacecraft and Rockets* 44 (1) (2007) 10–23.
- [8] S. J. Hughes, R. A. Dillman, B. R. Starr, R. A. Stephan, M. C. Lindell, C. J. Player, Inflatable re-entry vehicle experiment (IRVE) design overview, in: 18th AIAA Aerodynamics Decelerator Systems Technology Conference and Seminar, no. AIAA 2005-1636, 2005.
- [9] J. N. Moss, C. E. Glass, B. R. Hollis, Low-density aerodynamics of the inflatable re-entry vehicle experiment (IRVE), in: 44th AIAA Aerospace Sciences Meeting and Exhibit, no. AIAA 2006-1189, Reno, NV, USA, 2006.
- [10] S. O’Keefe, D. Bose, IRVE-II post-flight trajectory reconstruction, in: AIAA Atmospheric Flight Mechanics Conference and Exhibit, no. AIAA-2010-7515, 2010.
- [11] D. Jurewicz, G. Brown, B. Gilles, A. Taylor, R. Sinclair, B. Tutt, D. Lichodziejewski, C. Kelley, S. Hughes, Design and development of inflatable aeroshell structure for IRVE-3, in: 21st AIAA Aerodynamics Decelerator Systems Technology Conference and Seminar, no. AIAA 2011-2522, Dublin, Ireland, 2011.
- [12] E. H. Richardson, M. M. Munk, B. F. James, Review of NASA in-space propulsion technology program inflatable decelerator investments, in: 18th AIAA Aerodynamics Decelerator Systems Technology

- Conference and Seminar, no. AIAA 2005-1603, 2005.
- [13] I. G. Clark, J. R. Cruz, M. F. Hughes, J. S. Ware, A. Madlangbayan, R. D. Braun, Aerodynamic and aeroelastic characteristics of a tension cone inflatable aerodynamic decelerator, in: 20th AIAA Aerodynamics Decelerator Systems Technology Conference and Seminar, no. AIAA 2009-2967, Seattle, WA, USA, 2009.
- [14] K. Yamada, K. Suzuki, M. Hongoh, Aerodynamic characteristics of three-dimensional membrane aeroshells in supersonic flow, in: 21st Applied Aerodynamics Conference, no. AIAA 2003-3924, Orlando, FL, USA, 2003.
- [15] B. P. Anderson, Computational continuum and rarefied flow results for ballute applications, in: 42nd AIAA Aerospace Sciences Meeting and Exhibit, no. AIAA 2004-292, Reno, NV, USA, 2004.
- [16] J. McNamara, P. Friedmann, Aeroelastic and aerothermoelastic analysis in hypersonic flows: past, present, and future, *AIAA Journal* 49 (6) (2011) 1089–1122.
- [17] K. Takizawa, T. Spielman, C. Moorman, T. Tezduyar, Fluid-structure interaction modeling of spacecraft parachutes for simulation-based design, *Journal of Applied Mechanics-Transactions of the ASME* 79 (1) (2012) 010907.
- [18] T. Tezduyar, E. Levne, Parallel implementation of structural dynamic analysis for parachute simulation, *AIAA Journal* 45 (9) (2007) 2364–2364.
- [19] F. Schafer, S. Muller, T. Uffinger, S. Becker, J. Grabinger, M. Kaltenbacher, Fluid-structure-acoustic interaction of the flow past a thin flexible structure, *AIAA Journal* 48 (4) (2010) 738–748.
- [20] K. Takizawa, T. Spielman, T. Tezduyar, Space-time FSI modeling and dynamical analysis of spacecraft parachutes and parachute clusters, *Computational Mechanics* 48 (3) (2011) 345–364.
- [21] K. Takizawa, S. Wright, C. Moorman, T. Tezduyar, Fluid-structure interaction modeling of parachute clusters, *International Journal of Numerical Methods in Fluids* 65 (1-3) (2011) 286–307.
- [22] K. Karagiozis, R. Kamatoki, F. Cirak, C. Pantano, A computational study of supersonic disk-gap-band parachutes using large-eddy simulation coupled to a structural membrane, *Journal of Fluids and Structures* 27 (2011) 175–192.
- [23] C. Pantano, R. Deiterding, D. J. Hill, D. I. Pullin, A low numerical dissipation patch-based adaptive mesh refinement method for large-eddy simulation of compressible flows, *J. Comput. Phys.* 221 (1) (2007) 63–87.
- [24] F. Cirak, M. Ortiz, P. Schröder, Subdivision surfaces: A new paradigm for thin-shell finite- element analysis, *International Journal of Numerical Methods in Engineering* 47 (12) (2000) 2039–2072.
- [25] F. Cirak, M. Ortiz, Fully C^1 -conforming subdivision shell elements for finite deformation thin-shell

- analysis, *International Journal of Numerical Methods in Engineering* 51 (7) (2001) 813–833.
- [26] F. Cirak, M. West, Decomposition-based contact response (DCR) for explicit finite element dynamics, *International Journal of Numerical Methods in Engineering* 64 (8) (2005) 1078–1110.
- [27] A. Hutchings, R. Braun, K. Masuyama, Experimental determination of material properties for inflatable aeroshell structures, in: *20th AIAA Aerodynamics Decelerator Systems Technology Conference and Seminar*, no. AIAA 2009-2949, 2009.
- [28] D. I. Pullin, A vortex-based model for the subgrid flux of a passive scalar, *Physics of Fluids* 12 (2000) 2311–2319.
- [29] B. Kosovic, D. I. Pullin, R. Samtaney, Subgrid-scale modeling for large-eddy simulations of compressible turbulence, *Phys. Fluids*. 14 (4) (2002) 1511–1522.
- [30] S. T. Lundgren, Strained spiral vortex model for turbulent fine-structure, *Physics of Fluids* 25 (1982) 2193–2203.
- [31] D. I. Pullin, P. G. Saffman, Reynolds stresses and one-dimensional spectra for a vortex model of homogeneous anisotropic turbulence, *Phys. Fluids* 6 (1994) 1787–1796.
- [32] T. Voelkl, D. I. Pullin, D. C. Chan, A physical-space version of the stretched-vortex subgrid-stress model for large-eddy simulation, *Physics of Fluids* 12 (2000) 1810–1825.
- [33] D. J. Hill, C. Pantano, D. I. Pullin, Large-eddy simulation and multiscale modelling of a Richtmyer-Meshkov instability with reshock, *J. Fluid Mech.* 557 (2006) 29–61.
- [34] M. J. Berger, P. Colella, Local adaptive mesh refinement for shock hydrodynamics, *J. Comput. Phys.* 82 (1) (1989) 64–84.
- [35] M. Lombardini, Richtmyer-meshkov instability in converging geometries, Ph.D. thesis, Caltech (2008).
- [36] C. Pipkin, Relaxed energy densities for large deformation of membranes, *IMA Journal of Applied Mathematics* 52 (1994) 297–308.
- [37] H. Wagner, Flat sheet metal girders with very thin metal web, *Zeitschrift für Flugtechnik und Motorluftschiffahrt* 20.
- [38] Y. Wong, S. Pellegrino, Wrinkled membranes. Part I: experiments, *Journal of Mechanics of Materials and Structures* 1 (1) (2006) 1–23.
- [39] Y. Wong, S. Pellegrino, Wrinkled membranes. Part III: numerical simulations, *Journal of Mechanics of Materials and Structures* 1 (1) (2006) 61–93.
- [40] F. Cirak, Q. Long, Subdivision shells with exact boundary control and non-manifold geometry, *International Journal for Numerical Methods in Engineering* 88 (9) (2011) 897–923.
- [41] E. Onate, F. Zarate, Rotation-free triangular plate and shell elements, *International Journal For Nu-*

- merical Methods in Engineering 47 (2000) 557–603.
- [42] J. Kiendl, K.-U. Bletzinger, J. Linhard, W. R., Isogeometric shell analysis with Kirchhoff-Love elements, *Computer Methods in Applied Mechanics and Engineering* 198 (2009) 3902–3914.
- [43] D. Benson, Y. Bazilevs, H. M.-C., T. J. R. Hughes, A large deformation, rotation-free, isogeometric shell, *Computer Methods in Applied Mechanics and Engineering* 200 (2011) 1367–1378.
- [44] C. Farhat, K. van der Zee, P. Geuzaine, Provably second-order time-accurate loosely-coupled solution algorithms for transient nonlinear computational aeroelasticity, *Computer Methods in Applied Mechanics and Engineering* 195 (2006) 1973–2001.
- [45] R. Kirby, Z. Yosibash, G. Karniadakis, Towards stable coupling methods for high-order discretization of fluid-structure interaction: algorithms and observations, *J. Comput. Phys.* 2 (489-518).
- [46] R. Fedkiw, T. Aslam, B. Merriman, S. Osher, A non-oscillatory Eulerian approach to interfaces in multimaterial flows (the ghost fluid method), *Journal of Computational Physics* 152 (2) (1999) 457–492.
- [47] F. Cirak, R. Radovitzky, A Lagrangian-Eulerian shell-fluid coupling algorithm based on level sets, *Computers and Structures* 83 (2005) 491–498.
- [48] R. Deiterding, R. Radovitzky, S. P. Mauch, L. Noels, J. C. Cummings, D. I. Meiron, A virtual test facility for the efficient simulation of solid materials under high-energy shock-wave loading, *Engineering with Computers* 22 (3-4) (2006) 325–347.
- [49] F. Cirak, R. Deiterding, S. Mauch, Large-scale fluid-structure interaction simulation of viscoplastic and fracturing thin shells subjected to shocks and detonations, *Computers and Structures* 85 (11-14) (2007) 1049–1065.
- [50] L. Landau, L. Pitaevskii, E. Lifshitz, A. Kosevich, *Theory of elasticity*, Vol. 7, Butterworth-Heinemann, 1986.